geologicaacta

Citation: Travé, A., Nadal, J., Playà, E., Salas, R., Cantarero, I., Baqués, V., Cruset, D., Gomez-Rivas, E., Martín-Martín, J.D., 2025. Fracture-related dolostones replacing Upper Jurassic–lowermost Cretaceous syn-rift deposits in the eastern Iberian Chain (eastern Spain). Geologica Acta, 23.29, 1-pgs. DOI: 10.1344/GeologicaActa2025.23.29 Online ISSN: 1696-5728

ARTICLE IN PRESS

Fracture-related dolostones replacing Upper Jurassic–lowermost Cretaceous syn-rift deposits in the eastern Iberian Chain (eastern Spain)

Anna Travé[1] Judit Nadal[2] Elisabet Playà[1] Ramon Salas[1] Irene Cantarero[1] Vinyet Baqués[1] David Cruset[3] Enrique Gomez-Rivas[1] Juan Diego Martín-Martín[1]

[1]Departament de Mineralogia, Petrologia i Geologia Aplicada, Facultat de Ciències de la Terra, Universitat de Barcelona (UB), Institut de recerca Geomodels

Martí i Franquès, s/n. 08028 Barcelona. Spain. Travé E-mail: atrave@ub.edu, Playà E-mail: eplaya@ub.edu
Salas E-mail: ramonsalas@ub.edu, Cantanero E-mail: i_cantarero@ub.edu, Baqués E-mail: vbaques@ub.edu,
Gomez-Rivas E-mail: e.gomez-rivas@ub.edu, Martín-Martín E-mail: juandiegomartin@ub.edu

[2]Pasturalbosc

E-mail Nadal: judit@pasturabosc.cat

[3]Geociències Barcelona (GEO3BCN, CSIC)

Lluís Solé i Sabarís s/n, 08028 Barcelona. E-mail Cruset: dcruset@geo3bcn.csic.es

ABSTRACT

Upper Jurassic and Lower Cretaceous limestones and dolostones serve as hydrocarbon reservoirs in the offshore area of NE Spain. Since similar dolomitized rocks crop out in the adjacent onshore Maestrat Basin in the SE Iberian Range, understanding the dolomitization and other diagenetic processes is key to assessing reservoir properties. The Maestrat Basin dolostones crop out as elongated, asymmetric bodies, ranging from tens of centimetres to kilometres in length and up to 150m thick, with a wedge-shaped geometry closely associated with fractures. These dolostones are calcium-rich with low concentrations of Mn, Sr, and Na, but variable Fe, indicating that the replacement of the host limestone was followed by dolomite cement precipitation. Fluid inclusion data suggest that dolomitization took place at temperatures ranging between 70 and 120ºC. Such temperatures, together with the high $^{87}Sr/^{86}Sr$ ratio and fluid salinity (16 to 23% wt. NaCl equivalent), reveal that the dolomitization process took place in burial conditions, from fluids that were infiltrated and likely interacted with Triassic, Liassic, and basement rocks. Although the exact age of dolomitization is not fully constrained, it is thought to coincide with fault-related dolomitization events of the same type previously described in the Maestrat Basin, likely during the latest Early Cretaceous and/or during the Late Cretaceous, in relation to the post-rift basin stage. Geochemical differences between the depocenters and structural highs may reflect the controls of the Maestrat Basin basin architecture on the composition and distribution of fluids.

KEYWORDS **Fracture-related dolostones. Iberian Chain. Maestrat Basin. Upper Jurassic-lowermost Cretaceous. Isotope geochemistry.**

INTRODUCTION

Structural-controlled diagenetic alterations are common in extensional fault systems (Davies and Smith, 2006; Roure et al., 2005; Shelton et al., 2019). Among others, fault and fracture-related dolomitization of platform carbonates represent a frequent diagenetic alteration in sedimentary basins widely reported in the literature (i.e. Al-Aasm, 2003; Davies and Smith, 2006; Dewit et al., 2014; Esteban et al., 2005; Gomez-Rivas et al., 2014; Green and Mountjoy, 2005; Hollis et al., 2017; Humphrey et al., 2022; Machel, 2004; Machel and Mountjoy, 1987; Martín-Martín et al., 2013, 2015; Muñoz-Cervera and Cañaveras, 2023; Rustichelli et al., 2017; Sharp et al., 2010a; Wilson et al., 2007; Yao et al., 2020).

Fault-related dolostones typically replace limestones situated in the hanging walls of extensional or transtensional faults (Davies and Smith, 2006), although this is not always the case (e.g. Hirani et al., 2018). Numerous studies have shown that extensional faults act as preferential conduits for the circulation of hot, often hydrothermal, Mg-rich fluids which can percolate through sedimentary successions and trigger dolomitization reactions (i.e. Sharp et al., 2010b). The replacement of host carbonates can result in a variety of dolostone geobodies, which range between two end members based on their geometry (Humphrey et al., 2022; Yao et al., 2020). Massive (non-stratabound) dolostone geobodies typically develop close to and are distributed along faults or fault zones and dominantly replace carbonates without a textural or stratigraphic control (e.g. Black et al., 1981; Churcher and Majid, 1989; Dewit et al., 2014; Garreau et al., 1959; Gasparrini et al., 2006; Hollis et al., 2017; Jones, 1980; Malone et al., 1996; Sharp et al., 2010a; Stacey et al., 2021; Vandeginste et al., 2013; Wilson et al., 2007; Yao et al., 2020). Stratabound dolostone geobodies can extend away from fault planes following specific beds or stratigraphic units and mostly replace host carbonates with a textural control (e.g. Gasparrini et al., 2017; Gomez-Rivas et al., 2014; Hirani et al., 2018; Lapponi et al., 2011; Martín-Martín et al., 2013; Nader and Swennen, 2004; Sharp et al., 2010a). There are also situations in which both geometries are observed together, in a way that stratabound dolostone geobodies are connected to and thus sourced from massive dolostone patches (Yao et al., 2020). In addition to depositional facies, the stratabound morphology is thought to be enhanced by networks of bed-parallel stylolites (Gomez-Rivas et al., 2022; Martín-Martín et al., 2018).

The typical paragenesis associated with fault-related dolostones may include early calcite or dolomite cementation, one or several replacive and saddle dolomite phases, syntaxial dolomite overgrowths (i.e. overdolomitization), and post-replacement calcite cements, eventually followed by a mineralization stage (i.e. MVT-type deposits) (e.g. Gomez-Rivas et al., 2014; Lapponi et al., 2014; Martín-Martín et al., 2015). Dolostones can also be found replaced by calcite especially on outcrops, with the calcitization reaction being typically related to exhumation, exposure and circulation of meteoric fluids (Centrella et al., 2023a; Escorcia et al., 2013). Despite the above-mentioned literature, the formation of fault-related dolostones and controls on the replacement (i.e. depositional, diagenetic, and structural) are not completely constrained and new case studies are needed to increase our knowledge about such processes.

The Maestrat Basin, located in the SE Iberian Range (Spain), hosts numerous examples of fault-related dolostones (Caja et al., 2003; Marfil et al., 2005; Nadal, 2001; Salas, 1987). Among others, two exceptional seismic-scale case studies have been recently reported, both in Upper Jurassic (Serra d'Esparreguera; Humphrey et al., 2022) and Lower Cretaceous formations (Benicàssim; Centrella et al., 2023b; Corbella et al., 2014; Gomez-Rivas et al., 2014; 2022; Martín-Martín et al., 2013, 2015, 2018; Yao et al., 2020). These dolostones dominantly replace Upper Jurassic to Lower Cretaceous platform carbonates and have been considered outcrop analogues of offshore oil reservoirs in the western Mediterranean region (Lomando et al., 1993; Playà et al., 2010; Rodríguez-Morillas et al., 2013; Seemann et al., 1990), as well as in other parts of the Tethyan realm. In this regard, the Upper Jurassic Mas d'Ascla Formation was characterized as a source rock for the nearby Amposta oil field (Permanyer and Salas, 2005; Rossi et al., 2001; Salas and Permanyer, 2003). In addition, fault-related dolostones in the Maestrat Basin host MVT-type (Zn-Pb) mineralization (Grandia et al., 2003; Martín-Martín et al., 2015). While previous research has mainly concentrated on specific case studies, particularly dolostones replacing Lower Cretaceous rocks, have been extensively and thoroughly studied, dolostone bodies replacing Kimmeridgian–Berriasian limestones have received comparatively little attention. Furthermore, an integration of the occurrence of fault-related dolostones across the Maestrat Basin is lacking.

The main aim of this study is to report the occurrence of fault-related dolostones from the local to the basin scale within the uppermost Jurassic to lowermost Cretaceous carbonate succession of the Maestrat Basin. The specific objectives are: i) to describe the geometry and extent of fault-related dolostones from several outcrops, ii) to characterize the petrology of dolostones and their host rocks; iii) to characterize the geochemistry, elemental and isotope composition of dolomite and other diagenetic phases; and finally, iv) to establish a conceptual model for the formation of dolostones at the basin scale, including the role of faults and regional unconformities.

GEOLOGICAL SETTING

The Maestrat Basin is situated in the southeastern part of the Iberian Chain (Fig. 1), a mountain range that formed during the Paleogene inversion of the Mesozoic Iberian Rift System. The development of the rift system included six evolutionary stages (Salas *et al.* in Martín-Chivelet *et al.*, 2019): i) late Permian–Triassic Rifting, ii) Early and Middle Jurassic Post-rift, iii) Late Jurassic Rifting, iv) Neocomian (late Berriasian–Hauterivian) Post-rift, v) Early Cretaceous (Barremian–early Albian) Rifting, and vi) Late Cretaceous Post-rift. Following the Mesozoic extensional stages, the Iberian Rift System was inverted during the late Eocene to early Miocene, and subsequently affected by the late Oligocene to middle Miocene rifting that resulted in the opening of the western Mediterranean and the formation of the Valencia Trough (Salas and Casas, 1993; Salas *et al.*, 2001).

The Maestrat Basin formed during the Late Jurassic and Early Cretaceous rifting phases (Salas *et al.* in Martín-Chivelet *et al.*, 2019). These rifting phases coincided with extensional activity in the North Atlantic realm, culminating in the mid-Aptian separation of Iberia from North America and Europe, and the opening of the North Atlantic and Bay of Biscay oceanic basins (Salas *et al.*, 2001). The Maestrat Basin is bounded by normal faults organized into two main fault systems in the northern and southwestern sectors of the basin (Fig. 1). The northern faults are approximately E-W oriented and dip southwards, while the southern faults trend NW-SE and dip towards the NE and SW. The northern faults exhibit significantly greater displacement than the southern ones, resulting in an asymmetric basin with a main depocenter located in the north of the Maestrat Basin. The interaction of rollover structures in the hanging wall of these faults led to the development of several sub-basins named from north to south as: El Perelló, Morella, Oliete, La Salzedella, Las Parras, Penyagolosa, Cedramán, and Orpesa (Salas *et al.* in Martín-Chivelet *et al.*, 2019) (Fig. 1). Syn-rift deposits reach up to 4.3km in thickness in the main depocenter (La Salzedella sub-basin), whereas thicknesses drop below 100m, or are absent, beyond the fault zones to the north and south.

The Upper Jurassic to lowermost Cretaceous syn-rift sedimentation in the Maestrat Basin was dominated by shallow-marine platform carbonates (Fig. 2). Rapid subsidence of tilted fault blocks resulted in the drowning of an up to 50m thick Oxfordian shallow-water sponge-rich carbonate ramp (Iàtova Formation) and the accumulation of up to 800m of deep-water Kimmeridgian carbonate sediments (Polpís and Loriguilla formations). Thin-bedded lime mudstones and sponge buildups developed at the top of fault block crests (up to 500m high), transitioning vertically into anoxic basinal marls (Ascla Formation) in

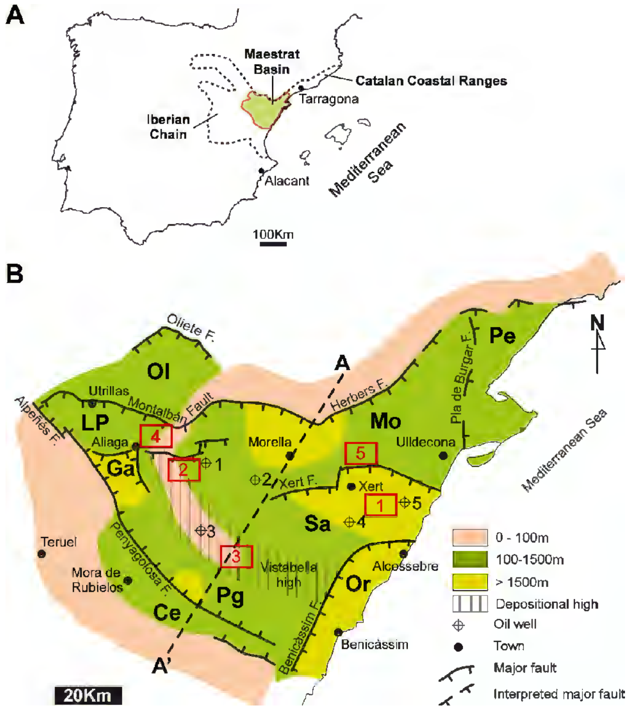

FIGURE 1. A) Map of the Iberian Peninsula showing the location of the Iberian Chain and Maestrat Basin. B) Simplified paleogeographic map of the Maestrat Basin during the Upper Jurassic–Lower Cretaceous rifting cycle showing the thickness of the corresponding succession and sub-basins (modified from Salas *et al.* in Martín Chivelet *et al.*, 2019 and Bover-Arnal *et al.*, 2024). Sub-basins are noted as: Pe (El Perelló); Mo (Morella); Ol (Oliete); LP (Las Parras); Sa (La Salzedella); Penyagolosa (Pg); Or (Orpesa); and Ce (Cedramán). Red squares and numbers represent studied areas (Table 1): La Salzedella (1); Bovalar (2); Alt Maestrat (3); Maestrat Occidental (4); Turmell-Ports de Beseit (5). Commercial oil-wells are noted as: 1 (Mirambell-1); 2 (Bovalar-1 and Bovalar-2); 3 (Maestrazgo-2); 4 (Salzedella-1); and 5 (Maestrazgo-1).

the subsiding hangingwall domains (up to 300m thick). The Tithonian to Berriasian interval comprises up to 1000m thick platform carbonates characterized by tidal flats and fringing oolitic-bioclastic shoals (Bovalar Formation) that grade basinwards into hemipelagic *Calpionella* limestones (La Pleta Formation). A regional unconformity (D3) marks the top of the Berriasian deposits. The lower Barremian succession is up to 1500m in thickness and is made of estuarine shallow-water carbonate platforms along the basin margins where carbonate production was dominated by molluscs and calcareous algae (Artoles Formation). Marginal oolitic-bioclastic shoals and coralgal boundstones are abundant. The upper Barremian is an up to 100m thick, tidal dominated lowstand delta complex, whose upper delta plain deposits contain abundant dinosaur remains (Morella Formation). During the uppermost Barremian and Aptian, widespread marine conditions favored the development of thick, prograding shallow-water carbonate platforms, up to 2km in total thickness, dominated by orbitolinids, calcareous algae, and rudists (Xert, Villarroya de los Pinares and Benassal formations). Within this succession, a marly

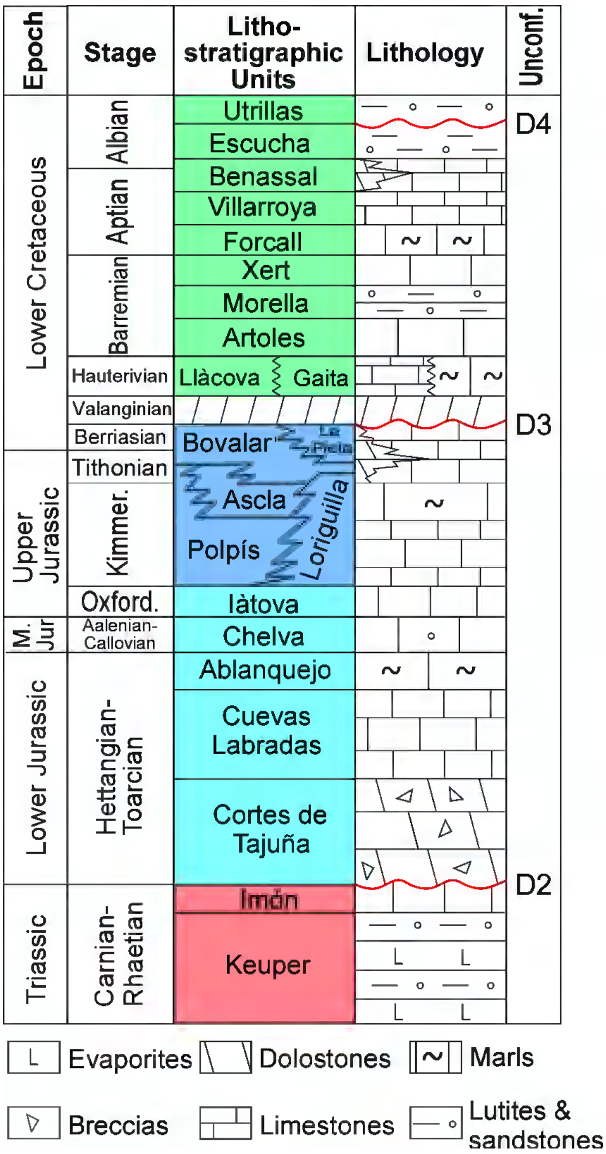

FIGURE 2. Simplified chrono- and lithostratigraphic chart of the Triassic to Cretaceous showing the age, formations, and lithology of the sedimentary succession in the Maestrat Basin (modified from Humphrey *et al.*, 2022). Major unconformities are noted as D2, D3 and D4.

interval belonging to the Forcall Formation is intercalated between the platform carbonates of the Xert and Villarroya de los Pinares formations (Fig. 2). The early to middle Albian interval comprises an extensive tidal-influenced delta system up to 500m thick, including abundant coal seams (Escucha Formation).

SAMPLES AND METHODS

Mapping of dolostone bodies was conducted in the uppermost Jurassic–lowermost Cretaceous Ascla, Bovalar, and La Pleta formations of the La Salzedella, Las Parras, and Morella sub-basins of the Maestrat Basin (Figs. 1; 2; Table 1). The host limestones and dolostones were systematically sampled at each outcrop for their petrological and geochemical characterization. Approximately 250 samples from dolostones and their host limestones were studied through polished slabs thin sections, both standard and dual-stained with Alizarin red S, using optical and cathodoluminescence microscopy. Cathodoluminescence analyses were carried out using a Technosyn Cold Model 8200MkII, operating at 12-17kV and 350μA gun current.

Twenty-five rock fragments and thin sections were carbon-coated for SEM-BSE observations, performed with a JEOL JSM-840, Cambridge Stereoscan S-120, and Hitachi S-2300 instruments. X-Ray Diffraction (XRD) was used to identify the major mineral phases in the collected samples.

Following the petrographic study, a selection of samples was analysed for geochemical characterization. A total of 40 carbon-coated thin sections were analysed using a CAMECA SX-50 electron microprobe equipped with four vertically arranged wavelength-dispersive X-ray spectrometers. Operating conditions included an excitation potential of 20kV, a beam diameter of 10μm, and current intensities of 10nA for Ca and Mg, and 50nA for Mn, Fe, Sr and Na. Detection limits were 765ppm for Ca, 395ppm for Mg, 180ppm for Mn, 275ppm for Fe, 280ppm for Sr and 200ppm for Na. The analytical precision for major elements averaged a standard error of 6.32% at a 3σ confidence level.

For stable isotope analysis of carbon and oxygen, a total of 106 samples (41 limestones and 65 dolostones) were separated using a dental microdrill. For limestones, we analysed the micrite matrix or the micritic components (ooids and peloids) in the grainstones. 0.5-1mg was reacted with 100% H_3PO_4 for 10min in vacuum at 90ºC. The resulting CO_2 was analysed using an on-line ISOCARB device coupled to a VG-Isotech SIRA II™ mass spectrometer. Isotopic values are reported in per mil relative to the Vienna-PDB standard, with a precision of ±0.02‰ for $\delta^{13}C$ and ±0.12‰ for $\delta^{18}O$. $\delta^{18}O$ and $\delta^{13}C$ isotope and electron microprobe analyses were carried out at the Scientific and Technical Centres of the University of Barcelona (CCiTUB).

In addition, 6 limestone, 11 dolostone and 4 anhydrite samples were analysed for their $^{87}Sr/^{86}Sr$ isotopic ratios. Powdered samples obtained by microdrilling were repeatedly leached with HCl of varying concentrations to produce chloride solutions. These were loaded into cation-exchange columns packed with DOVEX AG-50 resin, and strontium was isolated and loaded onto tantalum filaments for analysis with a VG Sector 54 multicollector mass spectrometer. Standards and reference material used —

DOI: 10.1344/GeologicaActa2025.23.29

Table 1. Studied geographic sectors and collected samples from the uppermost Jurassic–lowermost Cretaceous La Salzedella, Las Parras and Morella sub-basins (Maestrat Basin, southern Iberian Basin)

Sub-basin	Geographic area	Locality	Basin location	Host-limestone	Dolostone body geometry	Dolostone body geometry	Fault orientation	Samples
La Salzedella (Sa)	La Salzedella (1)	Alcalà de Xivert	depocenter	bottom Bovalar Fm.	Isolated fault-related wedge	100-meter-thick and approximately 600-meter-long	NE-SW-oriented normal fault	AX-01 / AX-29
		Sant Josep		top Ascla Fm. + Bovalar	Isolated fault-related wedge	50-meter-thick	NE-SW-oriented fault	BS-00 / BS-22
		Les Talaies		top Ascla Fm. + Bovalar	Massive	to 5km long, 2.5km-wide, and up to 150m-thick	WNW-ESE to NE-SW-oriented faults	FEJ-00 / FEJ-25 BA-1 / BA-10 MT-1 / MT-8
		Sta. Magdalena Polpís		bottom Bovalar Fm.	Isolated fault-related bodies	6 meter-long and up to 3.5 meter-thick	N-S faults	SMB-1 / SMB-10
	Bovalar (2)	Bovalar anticline	depositional high	Bovalar Fm.	Isolated wedges	up to 15 meter-thick	normal E-W fault dipping towards the south	BON-01 / BON-13
	Alt Maestrat (3)	Torre d'En Bessora	depositional high	top Bovalar Fm.	Massive	up to 70 meter-thick and up 800 meter-long	NE-SW steeply dipping towards the NNW	TB-01 / TB-12
		Tossal d'Orenga		top Bovalar Fm.	Repetition of isolated wedges	15 meter-thick	N-S faults	TO-01 / TO-17
		Coll del Vidre-Font de Molins		Bovalar Fm.	Isolated wedge	20 meter-long and up to 5 meter-thick	N-S oriented fractures	CV-01 / CV-12
		Coll del Vidre-Vistabella		Bovalar Fm.	Massive		large-scale E-W faults	AV-1 / AV-7
								CV-13 / CV-24
Las Parras (LP)	Maestrat Occidental (4)	Riu Bergantes	depositional high	Bovalar Fm.	Massive	difficult to observe		BG-01 / BG-08
		Barranc de Los Degollados-II		top Loriguilla Fm.	Isolated wedges	2 meter-thick		BD-02 / BD-10
		Barranc de Los Degollados-I		Bovalar Fm.	Isolated wedges	15-20 meter-thick		BD-11 / BD-19
		Jaganta-I		top Bovalar Fm.	Isolated wedges	2-10 meter-thick		JA-01 / JA-07
		Jaganta-II		Pleta Fm.	Isolated wedges			JA-08 / JA-15
Morella (Mo)	Turmell-Ports de Beseit (5)	El Turmell	depositional high	Bovalar Fm.	Massive in the lower part to stratabound in the upper part	18km long, 3km wide and 150m thick,	Footwall of the Turmell fault	TU-01 / TU-10
		Barranc del Racó del Patorrat		Bovalar Fm.	Massive in the lower part to stratabound in the upper part	up to 250 meters thick	E-W normal fault dipping towards the N	RP-01 / RP-15
		Els Mangraners		Bovalar Fm. + Pleta Fm.	Massive-stratabound	hectometric long and up to 80 meters thick	Close to the Herbers fault	MG-0 / MG-10
		El Parrisal-I		Bovalar Fm.	Massive			PA-0 / PA-03
		El Parrisal-II		Pleta Fm.	Isolated wedges			PA-04 / PA-06

NBS-987 and P450— yielded mean values of 0.710253 (n= 10) and 0.722482 (n= 4), respectively, with a reproducibility of ±3x10^{-5} and an analytical accuracy of 15x10^{-6}. All the results were normalised to $^{87}Sr/^{86}Sr$= 0.1194. $^{87}Sr/^{86}Sr$ analyses were carried out at the "C.A.I. de Geocronología y Geoquímica Isotópica" of the Universidad Complutense of Madrid.

Thin sections (100μm-thick) were prepared from 17 dolomite samples for microthermometric analysis of fluid inclusions. However, satisfactory measurements were obtained from only two samples, yielding data from 14 fluid inclusions. A Linkam THMS-600 heating-cooling stage was used, calibrated with distilled water (0.0ºC), pure CO_2 (-56.6ºC), and certified Merck melting point standards. Each inclusion was measured twice. Homogenization temperatures were not corrected for pressure. Measurement precision ranged from ±0.2ºC for freezing to ±2.0ºC for heating.

The geothermal gradient (G) during the Late Jurassic to Early Cretaceous rifting stage was calculated. The stretching factor (β) was previously estimated by Salas *et al.* (2001) based on subsidence data from several commercial oil wells in the Maestrat Basin, assuming uniform stretching and a pure shear model (McKenzie, 1978). The surface heat flow was estimated at 92mW/m^2, including a radiogenic contribution of ~12mW/m^2 from crustal rocks. The G value was obtained after applying the Fourier's Law:

$$HF= -KG$$

where HF is the surface heat flow, K is the thermal conductivity, and G is the geothermal gradient. A thermal conductivity value of 3.03W/mK was used (from the Maestrazgo-1 borehole; Fernández *et al.*, 1998). The resulting geothermal gradient is G= 30mK/m, equivalent to 30ºC/Km.

RESULTS

Geometry of dolostone geobodies

The studied dolostones dominantly replace limestones of the Tithonian and Berriasian Bovalar Formation and, to a minor extent, the laterally equivalent La Pleta Formation and the top of the Loriguilla Formation (Fig. 2; Table 1). The dolostone bodies are located adjacent to extensional fractures (both pure extensional fractures and vertical/subvertical normal faults), mostly striking NE-SW and, to a minor extent, NW-SE and N-S (Figs. 3; 4). The studied dolostone bodies show two main geometries: Massive and wedge-shaped bodies, and stratabound tabular bodies.

The massive and wedge-shaped dolostones form isolated and asymmetric bodies with a triangular geometry (wedge-shaped) attached to and extending away from faults and

FIGURE 3. Field views of the Thitonian–Berriasian limestones and dolostones in the La Salzedella sub-basin. A) Panorama of Tossal d'Orenga locality showing stratabound dolostones replacing the Bovalar Formation oncolitic limestones. B) Close view of A (red square) showing the wavy dolomitization fronts. C) Image of Tossal d'Orenga locality showing the sharp contact between limestones and dolostones. D) Close view of C showing a stylolitic plane forming a dolomitization front. E) Image of Torre d'En Bessora locality showing a massive dolostone body attached to a fracture plane. Note that the dolomitization front following the fault is not a discrete plane, suggesting that the fault postdates dolomitization.

fractures. Wedge-shaped massive dolostone bodies range from centimeters up to 600m in width and can reach up to 90m in thickness (Table 1). The replacement of the host limestones is generally pervasive near the fracture, does not follow specific facies beds, and gradually decreases away from it. A 0.5 to 2m-wide zone of dolomitic breccias, with abundant vuggy porosity, can sometimes be found in the vicinity of the fractures. Occasionally, the wedge-shaped dolostones are bounded by fractures in both sides.

The stratabound dolostones form continuous and elongated bodies with a tabular geometry that extends away from the wedge-shaped bodies (*i.e.* faults and fractures) following the bedding. Occasionally, the association of the stratabound bodies with the massive and wedge-shaped bodies, or with the fracture, is not observed. Frequently, several stratabound dolostone bodies appear in a single section at different stratigraphic positions. Despite being reported as stratabound, the dolomitization front typically

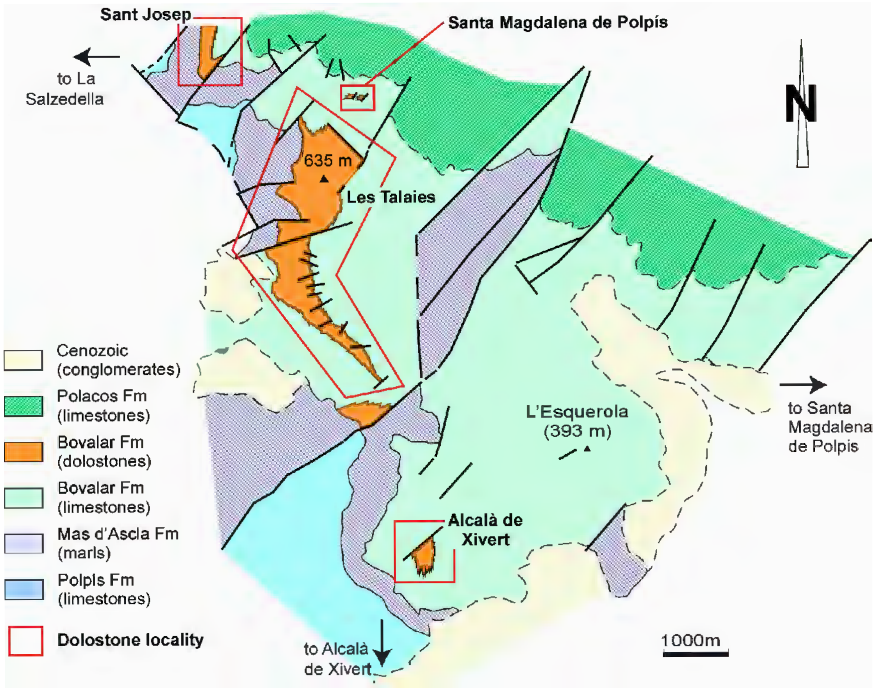

FIGURE 4. Geological map of the La Salzedella area showing the occurrence of several dolostone bodies associated with extensional fractures (Alcalà de Xivert, Les Talaies, Sta. Magdalena de Polpís and Sant Josep localities) (Table 1). Note how Les Talaies dolostone thins out of the fracture forming a stratabound body.

exhibits an undulated geometry, with vertical variations of several meters. The stratabound dolostones range from tens of meters to kilometers in width and can be up to 150m thick.

In both wedge-shaped and elongated stratabound dolostone geobodies, the contact between the dolostones and the host rocks is dominantly sharp, although a gradual transition between both lithologies is also observed. Sharp dolomitizing fronts typically coincide with bedding planes and stylolites (Fig. 3D). All the studied dolostones are stratigraphically located below the regional unconformity D3 (Fig. 2), which represents the upper boundary of the dolostone body in some cases, like the Tossal d'Orenga outcrop.

Petrology

Dolostones dominantly replace the Bovalar Formation but can also replace lateral equivalent limestones like the La Pleta Formation and stratigraphically lower limestones (Loriguilla Formation) (Fig. 2). The Ascla Formation is composed of basinal marls. The Bovalar Formation is organized into decimetre- to meter-thick shallowing-upward sequences, consisting of beds of wackestone, packstone and grainstone composed mainly of oncolites, peloids, ooids (Fig. 5A), dascycladacean and codiacean algae, benthic foraminifera, gastropods and bivalves. The La Pleta Formation is mainly composed of cyanobacterial limestones. Despite the textural variability among the precursor limestones affected by dolomitization, the resulting fabrics display similar petrographic features in all cases. Consequently, the different dolostone textures are described independently of their stratigraphic position (Fig. 5).

Dolomite occurs either as isolated rhombohedra, as replacive dolomite or as cement filling vuggy and fracture porosity. Replacive dolomite displays two different textures: replacive and saddle replacive . Similarly, there are two types of cement: dolomite cement and saddle dolomite cement.

Isolated dolomite rhombohedra are euhedral crystals, from 14 to 120μm in size, locally showing a zonation with a dark core and a clear outer rim, and exhibiting either non-luminescence or dull orange luminescence. The growth of these isolated dolomite crystals is non-selective but typically begins by replacing the micritic matrix (Fig. 5B), occasionally also replacing peloids and ooids. These rhombohedra can affect up to 25% of the host limestone and are mostly found away from fault planes and mainly in samples from the basin depocenter.

Replacive dolomite consists of subhedral to euhedral crystals, 14-400μm in size, commonly forming hypidiotopic crystal mosaics (Fig. 5C-E). Replacive dolomite pervasively

DOI: 10.1344/GeologicaActa2025.23.29

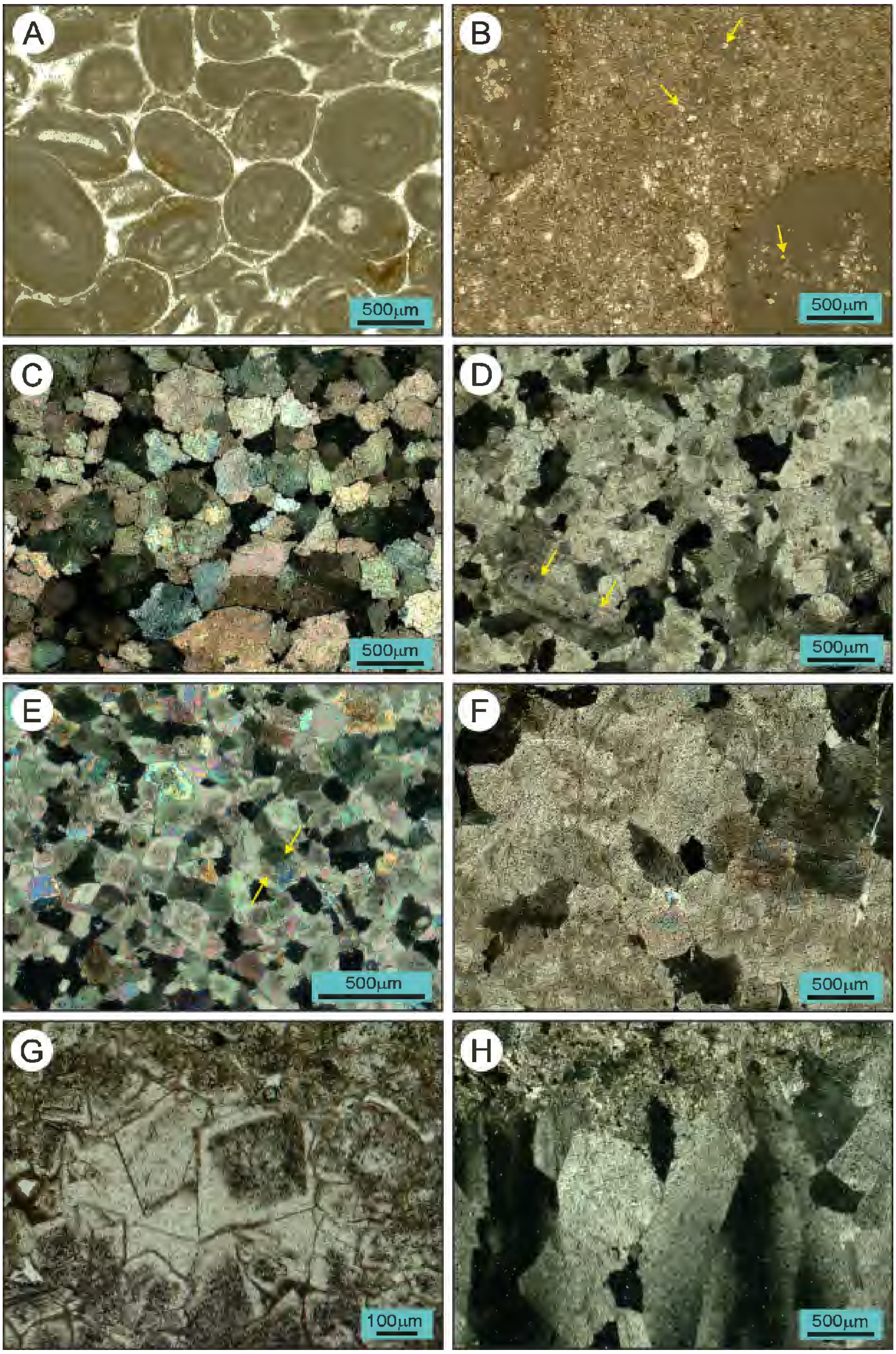

FIGURE 5. Photomicrographs of limestones and dolostones showing: A) Oolithic grainstone of the Bovalar limestones Formation affected by chemical compaction. Sample BON-12, La Salzedella sub-basin; plane-polarized light. B) Replacive pervasive and destructive dolomite Morella sub-basin, sample RP-10; crossed-polars. C) Replacive pervasive and partially destructive dolomite with hypidiotopic texture and oolith ghosts (see arrows). La Salzedella sub-basin, sample TB-17; crossed-polars. D) Replacive dolomite consisting of crystals with a clearer outer part and darker nucleus, which can be interpreted as oolith ghosts (see arrows). La Salzedella sub-basin, sample AX-7; crossed-polars. E) Isolated dolomite rhombohedra replacing a peloidal-ooidal wackestone; rhombohedra crystals are more abundant in the micritic matrix. Sample BON-11, La Salzedella sub-basin; plane-polarized light. F) Saddle replacive dolomite. La Salzedella sub-basin, sample TB-08; crossed-polars. G) Dolomitic cement showing darker nucleus and filling a microvug. Morella sub-basin, sample MG-0; crossed-polars. H) Saddle dolomitic cement inside a vug porosity. La Salzedella sub-basin, sample TB-15; crossed-polars.

replaces all components of the host limestones (*i.e.* matrix, grains and early cements). The replacement is mostly destructive (Fig. 5C), although partially destructive or non-destructive fabrics (*i.e.* mimetic) are also observed (Fig. 5D). The crystal size tends to decrease with increasing distance from fractures. Some crystals are zoned when observed with the optical microscope, displaying a darker core and a clear outer rim (Fig. 5E), both showing a homogeneous dull orange luminescence.

Saddle replacive dolomite consists of subhedral to anhedral crystals, 100μm to 1mm in size, giving rise to xenotopic to hypidiotopic crystal mosaics. The replacement is pervasive and mostly destructive (Fig. 5F). The crystals exhibit undulose extinction and homogeneous dull orange luminescence.

Dolomite cement consists of euhedral crystals, 20-400μm in size, growing in optical continuity with the host replacive dolomite and fills vuggy and fracture porosities. Crystals are zoned, with a dark core (dull orange luminescence) and a clear rim (dull orange to bright yellow zoned luminescence) (Fig. 5G).

Saddle dolomite cement is composed of euhedral crystals, 250μm to 2-5mm in size, with curved faces and curved cleavage planes, filling vuggy and fracture porosities (Fig. 5H). The crystals display wavy extinction and homogeneous dull orange luminescence, although a locally developed bright luminescent outer rim may also occur.

Stoichiometry and elemental geochemistry

The stoichiometry and the elemental composition are quite similar across all the studied dolostones, regardless of texture, geographic sector, or stratigraphic position.

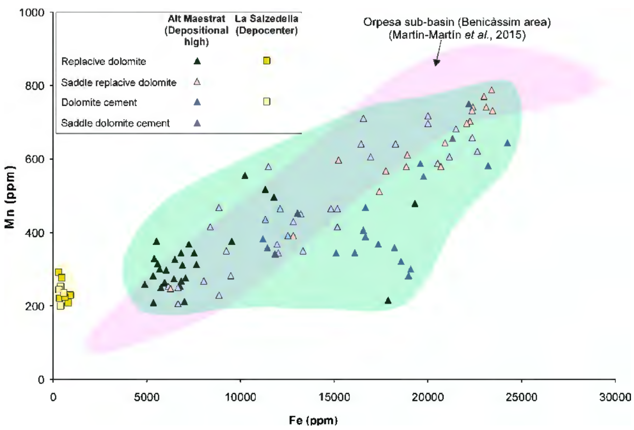

FIGURE 6. Fe *versus* Mn cross-plot showing the different replacive dolomite and dolomite cement phases from the La Salzedella sub-basin (La Salzedella and Alt Maestrat areas).

TABLE 2. Synthesis of the stoichiometry and elemental composition of the replacive dolomite and the different dolomite cement types

Texture		$CaCO_3$ (%)	$MgCO_3$ (%)	Mn (ppm)	Fe (ppm)	Sr (ppm)	Na (ppm)
	M	57.1	45.3	-	1070	-	-
Isolated	m	53.7	42.0	-	<b.d.l.	-	-
dolomite	mv	55.2	43.6	-	-	-	-
rhombohedra	σ	0.7	0.4	-	-	-	-
	n	27	27	-	9	-	-
	M	70.5	45.0	550	19300	383	539
Replacive	m	49.6	29.4	<b.d.l.	<b.d.l.	66	<b.d.l.
dolomite	mv	55.5	42.7	-	-	80	-
	σ	1.5	1.6	-	-	25	-
	n	403	403	80	163	5	2
	M	55.9	46.2	1680	23460	-	360
Saddle	m	52.6	37.6	<b.d.l.	660	-	<b.d.l.
replacive	mv	54.2	42.4	-	7900	1120	-
dolomite	σ	0.7	2.6	-	8480	-	-
	n	54	54	30	54	1	3
	M	64.8	45.6	810	25300	1030	334
Dolomite	m	53.6	33.7	<b.d.l.	<b.d.l.	<b.d.l.	<b.d.l.
cement	mv	57.1	40.0	-	-	-	-
	σ	1.2	1.2	-	-	-	-
	n	222	222	33	39	5	5
	M	58.3	45.9	720	22630	-	1090
Saddle	m	44.5	34.1	<b.d.l.	1030	-	<b.d.l.
dolomite	mv	54.2	42.3	-	7590	-	-
cement	σ	1.6	2.3	-	6225	-	-
	n	84	84	50	83	-	4

b.d.l.: below detection limit
M: Maximum value. m: minimum value; mv: mean value. S: Standard deviation. n: number of analized spots

However, minor differences are observed. The studied dolostones are non-stoichiometric, calcium-rich (Ca_{50-70}–Mg_{30-46})CO_3, with an average of approximately 43% molar of $MgCO_3$. Only the dolomite cement is slightly more depleted in magnesium compared to the other dolostone textures, with an average of 40% molar of $MgCO_3$ (Table 2). Dolostones show variable Fe contents but low Mn, Sr and Na contents (Table 2). The most relevant differences are observed in the La Salzedella sub-basin between samples from depositional highs and those from depocenter (Fig. 6). The highest Fe and Mn contents are found in samples from the Alt Maestrat sector (depositional high), with Fe contents reaching up 23460ppm (4.9mol % $FeCO_3$) in replacive dolostones and up to 25300ppm (5.2mol % $FeCO_3$) in dolomite cements. Mn contents reached up to 1680ppm, showing a good positive correlation between Fe. In contrast, the replacive dolostones from the La Salzedella sector (depocenter), are depleted in both Fe and Mn.

Oxygen and carbon isotopes

The uppermost Jurassic–lowermost Cretaceous host-limestones in the Maestrat Basin have $\delta^{18}O$ values ranging from -8.1 to -0.1‰ VPDB and $\delta^{13}C$ values ranging between -6.6 and +2.3‰ VPDB (Table 3). Isotopic variations are observed depending on their

TABLE 3. Oxygen and carbon isotope compositions of the uppermost Jurassic–lowermost Cretaceous dolostones from the Maestrat Basin

Texture	Sample	$\delta^{18}O_{VPDB}$ (‰)	$\delta^{13}C_{VPDB}$ (‰)
	DOLOMITES		
Replacive dolomite	MT-6	-4.9	+1,6
	MT-8	-7.0	+2,1
	AX-07	-4.6	+1,3
	AX-10.1	-7.1	-1,6
	AX-12	-5.9	-0,7
	AX-14.1	-5.8	-1,3
	AX-14.3	-5.6	+1,1
	AX-15	-5.8	+1,6
	AX-16	-9.8	-2,5
	AX-17	-5.0	+1,5
	AX-21	-6.1	+2,4
	AX-22	-3.8	+1,7
	AX-25	-4.7	+1,5
	BS-3	-7.5	+2,2
	BS-4	-6.3	+2,0
	BS-7	-6.2	+0,8
	BS-8	-5.2	+0,9
	BS-11	-6.5	-0,4
	FEJ-13	-7.2	+1,9
	FEJ-15	-4.4	+2,3
	FEJ-16	-8.4	+2,4
	FEJ-17.1	-5.8	+1,8
	SMB-2	-7.9	+0,2
	SMB-05	-6.9	+1,5
	SMB-06	-6.5	+0,5
	SMB-09	-6.1	+1,6
	BA-1	-6.2	+1,4
	BA-2	-6.9	+1,8
	BA-6	-6.8	+1,4
	BA-7	-3.7	+2,1
	BON-01	-6.8	+1,8
	BON-05	-9.5	+2,0
	TO-04	-6.6	-2.1
	TB-05	-5.9	+1,9
	TB-12	-6.6	-1.9
	CV-05	-7.4	+0,1
	AV-5-1	-5.2	+2,1
	AV-5-2	-4.9	-1.2
	AV-7	-5.4	+2,2
	CV-13	-5.7	+1,5
	CV-14	-6.1	+1,1
	CV-15A	-5.9	+1,6
	CV-15C	-7.4	+0,2
	CV-16	-5.2	-2.2
	CV-17-1	-6.7	+2,0
	CV-17-2	-5.5	+2,3
	CV-23	-7.0	-0.9
	CV-24	-7.4	+0,3
	BD-13	-1.3	+1,4
	BG-08	-5.7	+0,6
	BD-03	-4.3	+0,7
	BD-04	-4.0	+0,2
	BD-06(b-2)	-2.4	-0.1
	PA-00	-4.3	-3.5
	PA-01	-4.1	-3.9
	PA-02	-4.1	-3.3
	MG-01	-5.6	-1.2
	RP-01	-2.9	+0,3
	RP-02	-4.0	-1.5
	RP-04	-3.1	-1.5
	RP-06	-4.5	-1.1
	RP-08	-3.1	-0.7
Saddle replacive	TB-08	-6.7	+1,7
dolomite	CV-09	-6.4	+2,3
Dolomite cement	SMB-5B	-9.5	+0,7

stratigraphic position and across different sub-basins, reflecting the variable nature of the analysed material (Figs. 7; 8). The $\delta^{18}O$ and $\delta^{13}C$ values of these limestones are lighter than those typically reported for uppermost Jurassic (Tithonian) and Cretaceous marine limestones (-6 to +1.5‰ VPDB for oxygen and -3 to +4.5‰ VPDB for carbon; Groetsch and Vahrenkamp, 1995; Jenkyns *et al.*, 2002; Morrison and Veizer, 1990; Pirrie and Marshal, 1990).

The oxygen and carbon isotope compositions of the replacive dolostone range from -9.8 to -1.3‰ and from -3.9 to +2.4‰ VPDB, respectively (Table 3). The saddle replacive dolostone and dolomite cement samples exhibit isotopic compositions within the same range as the replacive dolostone. Dolostones replacing all Tithonian–Berriasian limestones yield similar isotopic compositions (Fig. 7; 8), suggesting a widespread dolomitization process. In the La Salzedella sub-basin, the $\delta^{18}O$ values of both replacive dolomite and saddle replacive dolomite are approximately 2-3‰ lighter than those of the precursor limestones (Figs. 7; 8).

When comparing samples from different paleogeographic settings, dolostones located in the depocenter (La Salzedella sector) show a wider range of $\delta^{18}O$ compositions (up to 6‰ variation), whereas dolostones from the high depositional areas display a narrower $\delta^{18}O$ variation of 2-4‰ (Figs. 7; 8). In the Las Parras and Morella sub-basins, both the precursor limestones and dolostones exhibit similar isotopic ranges (Figs. 7; 8). Likewise, dolostones from different sub-basins also shows distinct isotopic trends: the La Salzedella sub-basin records the lightest $\delta^{18}O$ values, with a mean value of -6.3‰, while the Las Parras and Morella sub-basins show mean values of -3.5 and -4‰, respectively. In contrast, $\delta^{13}C$ values are heavier in the Las Parras sub-basin (mean of +0.6‰) compared to the Morella sub-basin (mean of -1.6‰). These differences suggest local variations in the source of the bicarbonate ions (possibly influenced by the input of biogenic HCO_3^-) in the dolomitizing fluids.

Strontium isotopes

The $^{87}Sr/^{86}Sr$ ratios of the bulk limestones range from 0.70721 to 0.70786 (mean of 0.70741, Table 4), slightly higher than the strontium isotope values of Jurassic–Early Cretaceous seawater (0.7068-0.7074, after Burke *et al.*, 1982; Jenkyns *et al.*, 2002; Jones *et al.*, 1994; Koepnick *et al.*, 1985; Veizer and Compston, 1974; Veizer *et al.*, 1997). The $^{87}Sr/^{86}Sr$ ratios of the replacive dolostones are more radiogenic than those of the limestones, ranging from 0.70740 to 0.70798, with a mean of 0.70760 (Fig. 8). These values are comparable to the range reported for

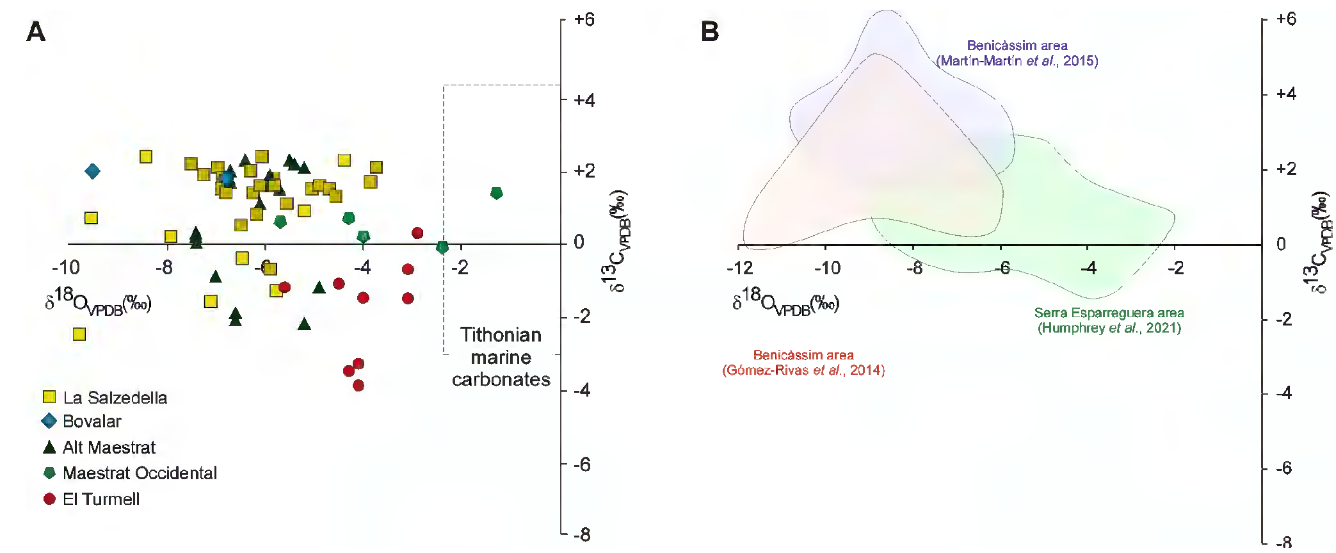

FIGURE 7. A) Oxygen and carbon isotope compositions of Upper Jurassic–Lower Cretaceous dolostones from the Maestrat basin. B) Oxygen and carbon isotope compositions of dolostones from Benicàssim and Serra d'Esparreguera nearby areas.

Triassic–Early Jurassic seawater (0.7075-0.7082, after Faure *et al.*, 1978; Holser and Magaritz, 1987; Koepnick *et al.*, 1990; Korte *et al.*, 2003; Veizer *et al.*, 1997). To further compare and discuss the $^{87}Sr/^{86}Sr$ values of dolostones, we also analysed Triassic and Lower Jurassic marine-precipitated anhydrites from the Maestrat and Valencia-Cuenca basins (Table 5), which display similar $^{87}Sr/^{86}Sr$ ratios to the studied dolostones (0.7073-0.7080; Fig. 8).

Fluid inclusions

The measured fluid inclusions within the replacive dolomite are primary in origin, biphasic (liquid-vapour), range in size from 3 to 10μm, and show no evidence of necking. They are mainly located along growth planes in the outer parts of the dolomite crystals. Homogenization temperatures (Th) range from 70 to 120ºC (n= 14, with a mean of ≈102, a standard deviation of 13,5; Table 6), indicating the involvement of hot fluids. Eutectic

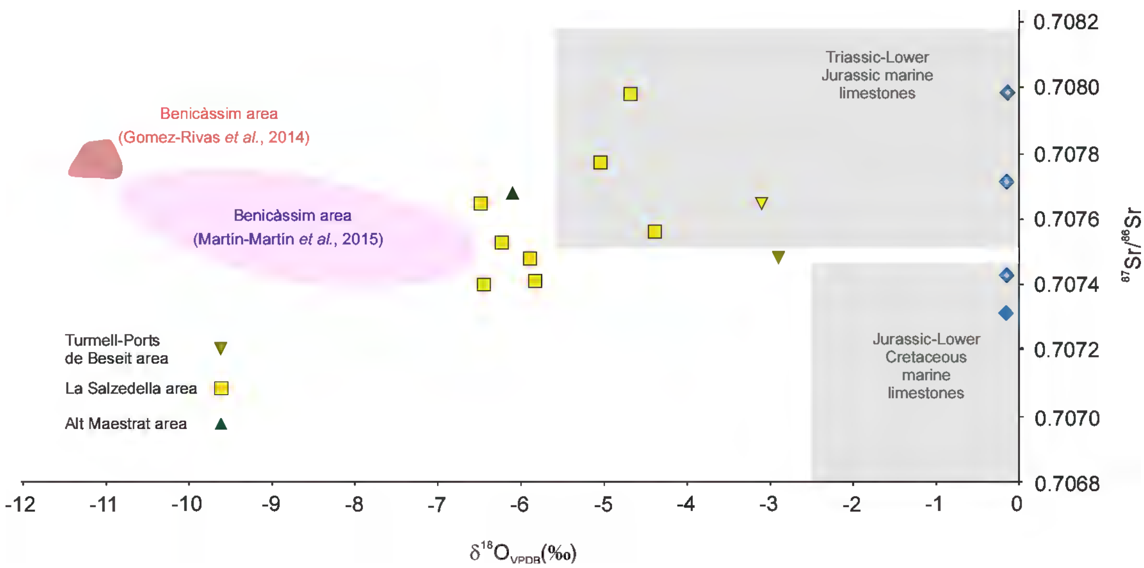

FIGURE 8. Oxygen *versus* strontium isotopy of Upper Jurassic–lowermost Cretaceous dolostones from the Maestrat Basin. Strontium isotope ratios of Triassic and Lower Jurassic anhydrites from the Valencia-Cuenca and Maestrat basins are included (blue diamonds). Note that the oxygen signatures of the anhydrites are not plotted.

TABLE 4. Strontium isotope composition of the uppermost Jurassic–lowermost Cretaceous dolostones from the Maestrat Basin

Lithology/Texture	Sample	$^{87}Sr/^{86}Sr$
Limestones	RP-14	0.70742 (±6)
	MG-04	0.70742 (±5)
	AX-19	0.70721 (±13)
	AX-27A	0.70733 (±6)
	BA-10	0.70724 (±6)
	CV-02	0.70786 (±5)
Replacive dolomite	RP-01	0.70748 (±6)
	RP-04	0.70765 (±5)
	FEJ-15	0.70756 (±19)
	FEJ-17	0.70741 (±6)
	BS-11	0.70740 (±7)
	AX-12	0.70748 (±6)
	AX-17	0.70777 (±11)
	AX-25	0.70798 (±11)
	SMB-6	0.70765 (±9)
	BA-1	0.70753 (±10)
	CV-17	0.70768 (±5)

temperatures (Te) of the fluid inclusions vary between -60 and -50ºC (n= 9, with a mean of ≈55, a standard deviation of 3,3; Table 6), consistent with the eutectic temperature of the NaCl-$CaCl_2$-$MgCl_2$-H_2O system (Davis *et al.*, 1990; Sheperd *et al.*, 1985; Zwart and Touret, 1994). Final ice melting temperature (Tmi) ranges from -10 to -21ºC (n= 11, with a mean of ≈16,7, a standard deviation of 3,1; Table 6, corresponding to water salinities of 16-23wt % NaCl equivalent (Allan and Wiggins, 1993; Crawford, 1981). The Tmi-Th plot (Fig. 9) forms a tight cluster, suggesting that the measurements were taken from unaltered fluid inclusions (Allan and Wiggins, 1993).

TABLE 5. Strontium isotope composition of the Triassic–Lower Jurassic anhydrite from the Maestrat and Valencia-Cuenca basins

Age	Basin	Core	Sample	$^{87}Sr/^{86}Sr$
Top of Upper Liassic	Valencia-Cuenca	Carcelén-1	CAR-5	0.70729
Lower Liassic			CAR-11	0.70742
Lower Liassic			CAR-12	0.70766
Middle Muschelkalk	Maestrat	Bovalar-1	BOV-11	0.70796

DISCUSSION

Geometry and distribution of fracture-related dolostones

Massive dolostones are common alteration products formed during fracture-related diagenesis, where fractures act as conduits for the migration of magnesium-rich fluids that replace the host limestones without a facies or texture control (*i.e.* non-stratabound). In these scenarios, dolostones form massive bodies or patches, eventually wedge-shaped, attached to fracture planes or zones with the degree of replacement decreasing away from the fracture (*e.g.* Black *et al.*, 1981; Churcher and Majid, 1989; Dewit *et al.*, 2014; Garreau *et al.*, 1959; Gasparrini *et al.*, 2006; Jones, 1980; Hollis *et al.*, 2017; Malone *et al.*, 1996; Sharp *et al.*, 2010a; Stacey *et al.*, 2021; Vandeginste *et al.*, 2013; Wilson *et al.*, 2007; Yao *et al.*, 2020). Eventually, the dolomitizing fluids circulate along specific facies beds with textures resulting in the transition from massive to stratabound bodies (*e.g.* Gasparrini *et al.*, 2017; Gomez-Rivas *et al.*, 2014; Hirani *et al.*, 2018; Lapponi *et al.*, 2011; Martín-Martín *et al.*, 2013; Nader and Swennen, 2004; Sharp *et al.*, 2010a).

In a similar way to the above-mentioned scenario, the dolostones replacing the Tithonian–Berriasian limestones

TABLE 6. Homogenization (Th), eutectic (Te) and final melting ice (Tmi) temperatures of primary and biphasic fluid inclusions of replacive dolomite *s.s.* from the La Salzedella sub-basin (Maestrat Basin)

Palaeogeographic position	Sector	Sample	Spots	Th (ºC)	Te (ºC)	Tmi (ºC)
Depositional High	Alt Maestrat	CV-5	#1	95	±-60	-18.5
			#2	96.9	<-50	-20.9
			#3	98.6		
Depocenter	La Salzedella	MT-6	#1	99.5	-53/-54	-16.4
			#2	69.4	-53/-54	-16.4
			#3	111.7	<-53	-20.5
			#4		-59	-16.6
			#5	104.3	-58.1	-15.9
			#6	85.5		
			#7	> 120		-14.9/-9.3
			#8	117/120		-16.1
			#9	> 114		
			#10	102.5		
			#11	100		-18.5

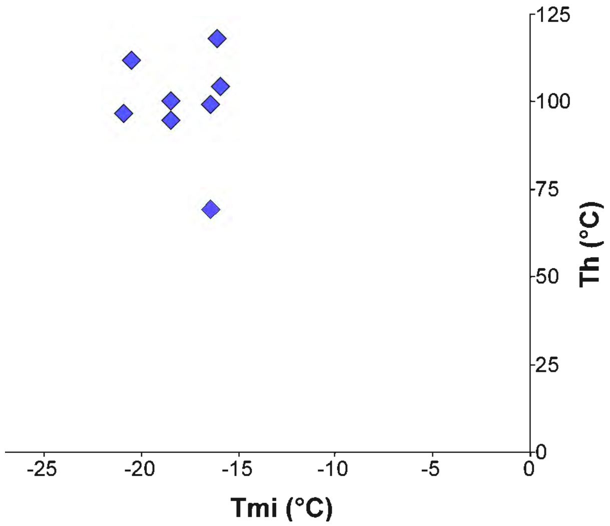

FIGURE 9. Tmi-Th plot of primary and biphasic fluid inclusions of replacive dolomite from the La Salzedella sub-basin (Maestrat Basin).

studied here display two main geometries directly related to their proximity to fractures. The wedge-shaped massive dolostones bodies represent the replacement of the host limestones in the vicinity of the fracture where the host limestones are pervasively dolomitized without textural or facies control (Fig. 3E). By contrast, the stratabound and tabular dolostone bodies represent the replacement of the host limestones away from the faults where fluids focused along specific beds, or set of beds, with the highest porosity and permeability at time of dolomitization. The occurrence of these two types of dolostone bodies is exemplified in the geological map of the La Salzedella area (La Salzedella sub-basin) (Fig. 4). There, massive wedge-shaped bodies with diverse size (meters to hundreds of meters) are closely associated with SE-NW striking fractures (Sant Josep, Santa Magdalena de Polpís and Alcalà de Xivert localities), suggesting that this fault system partially controlled the replacement of the Tithonian–Berriasian limestones. However, the large dolostone body (Les Talaies locality) is associated with a NW-SE striking fault, showing a massive wedge-shaped geometry attached to the fault and a stratabound geometry away from. This dolostone body is up to 5km long, suggesting that NW-SE faults are the most important fractures controlling the dolomitization of the Tithonian–Berriasian limestones.

Most of the studied dolostone bodies are significantly smaller to other case studies of fault-related dolostones from the Maestrat Basin reported in the literature. This is the case of Serra d'Esparreguera (La Salzedella sub-basin) where dolostones replacing Kimmeridgian to Berriasian sediments (Polpís and Bovalar formations) form a single seismic-scale tabular and elongated stratabound geobody with a lateral extension of 3.1km and a thickness up to 245m (Humphrey *et al.*, 2020). According to the previous authors, dolostones are distributed parallel to, and thus associated with, large (*i.e.* kilometric-scale) Mesozoic NE-SW faults. Similarly, dolostones replacing upper Aptian to lowermost Albian carbonates in the Benicàssim area (Orpesa sub-basin) form several stratabound tabular bodies that extend up to 7km and up to 125m in thickness (Martín-Martín *et al.*, 2013). These authors reported that dolostones are associated with the intersection of basement Mesozoic NW-SE and NE-SW faults. In both case studies the large extension and thickness of the dolostone bodies are likely related to syn-rift regional faults affecting the basement.

The close relationship between faults and fractures and dolostone geobodies indicates that such structures represent the primary control on dolomitization of the Tithonian–Berriasian limestones studied in this work (Figs. 1; 3). Specifically, the geometry of the dolostones with a massive wedge-shaped (*i.e.* non-stratabound) body attached to fracture planes and a stratabound body away from faults planes evidence that faults and fractures were the conduits of Mg-rich dolomitizing fluids (Martín-Martín *et al.*, 2015).

Abrupt and sharp diagenetic fronts (dolomitization fronts) between dolostones and host limestones like those described in the studied area are typically reported in replacive burial dolostones (Warren, 2000; Machel, 2004). This is also the case in other studies reported from the Maestrat Basin, such as the Thitonian–Berriasian Bovalar Formation in the La Salzedella sub-basin (Humphrey *et al.*, 2022) and the late Aptian–earliest Albian Benassal Formation in the Orpesa sub-basin (Martín-Martín *et al.*, 2013, 2015) (Figs. 1; 2), as well as in studies worldwide (Mozafari *et al.*, 2019; Wilson *et al.*, 1990). In the studied area, the diagenetic fronts commonly coincide with bedding-planes suggesting facies and or texture control on dolomitization (Martín-Martín *et al.*, 2015). Similar to bedding-planes, bed-parallel stylolitic surfaces and/or amalgamated stylolite systems are also reported to form common dolomitization fronts (Gomez-Rivas *et al.*, 2022; Humphrey *et al.*, 2022; Martín-Martín *et al.*, 2018). These authors concluded that both bedding planes and stylolites represent bounding surfaces enhancing the stratabound distribution of dolostones.

Dolomitization conditions

The occurrence of euhedral dolomite crystals (*i.e.* planar-e) replacing the micritic matrix is interpreted to be the first stage of dolomitization of the studied Tithonian–Berriasian limestones (Fig. 5A-B). Mimetic fabrics in replacive dolomite indicate that the replacement of the host limestone occurred after some burial (Fig. 5D).

The petrography and geochemistry of the studied dolostones (Fig. 5) can be interpreted as the result of multiple dolomitization events at various temperatures, from fluids with variable $\delta^{18}O$ values and/or by variable fluid-rock ratios. Dolomitization of the precursor limestone and precipitation of dolomite cements within the rock pore space likely gave rise to: i) a complex association of replacive dolomite, saddle replacive dolomite, dolomite cement and saddle cement and ii) optical continuity between the replacive dolomite and dolomite cement and between saddle replacive dolomite and saddle dolomite cement in the vuggy and fracture porosity. Replacive dolomitization of the host limestone occurred before saddle dolomite cementation, as has been commonly observed in numerous hydrothermal dolomite settings (as summarized in *e.g.* Davies and Smith, 2006). Both processes are interpreted to be closely linked genetically, with a common fluid origin and with both processes occurring roughly at the same time.

The $\delta^{18}O$ signature varies across the study areas, with more negative values at the basin depocenter (La Salzedella) compared to those measured in the depositional highs. This spatial distribution of the isotopic values likely indicates a higher burial depth, and therefore higher fluid temperatures, at the depocenter compared to the sub-basin margins. On the other hand, the $\delta^{13}C$ values are relatively similar, although there are some small differences between the different study areas. The lighter $\delta^{13}C$ signature of the El Turmell dolomite is probably due to partial calcitization of dolomite crystals associated with meteoric fluids, observed in thin sections and SEM analyses (Fig. 7). The studied dolostones have similar $\delta^{18}O$ signatures to those of the Bovalar Formation in the Serra d'Esparreguera area (Fig. 7; Humphrey *et al.*, 2022), but are heavier than the replacive dolostones and saddle dolomite cements described in other parts of the Maestrat Basin (*e.g.* in the Penyagolosa sub-basin; Gomez-Rivas *et al.*, 2014; Martín-Martín *et al.*, 2015, 2018; Fig. 7). This may also indicate that the Penyagolosa dolostones would have formed from warmer fluids.

The higher content of Fe and Mn in the dolostones located in the depositional highs compared to those from the basin depocenter indicates higher contribution of fluids that have interacted significantly with basin rocks (Gregg and Sibley, 1984).

The youngest limestone unit affected by dolomitization (Bovalar Formation) was deposited between approximately 148 and 142Ma, during the middle Tithonian to lower Berriasian, based on the presence of the foraminifer *Anchispirocyclina lusitanica* (Bádenas *et al.*, 2004). In the Tossal d'Orenga outcrop (La Salzedella sub-basin, Table 1), the dolomitized section is affected by an erosive surface (the so-called D3 regional unconformity), above which freshwater non-dolomitized limestones with charophytes of Valanginian–early Hauterivian age were deposited. On top of these freshwater limestones, the Upper Hauterivian marine deposits (Gaita Formation; Neuman, 1987) are dated as ~134Ma (based on ammonites, Gradstein *et al.*, 2004). However, this unit is not affected by dolomitization, revealing that if replacement postdates the D3 unconformity such structure likely acted as a regional seal to constrain replacement to the Berriasian and older rocks. A similar observation was made at the Benicàssim area (Penyagolosa sub-basin), where the regional unconformity D4 acted as a regional seal for the fluids responsible for the dolomitization of middle Aptian to lowermost Albian carbonates (Yao *et al.*, 2020; Fig. 2).

Although no absolute ages have been published for the studied dolostones, the dolomite textures, paragenesis, and geochemical data presented here are very similar to those reported from the Serra Esparreguera area, which affects the same Bovalar Formation (La Salzedella sub-basin, Humphrey *et al.*, 2022), as well as to those affecting the Aptian–Albian deposits in the Penyagolosa sub-basin (Martín-Martín *et al.*, 2015, 2018), suggesting a comparable origin and age. The presence of dolostone geobodies of similar characteristics just below the regional unconformity D3 (replacing Tithonian–Berriasian rocks) and just below the regional unconformity D4 (replacing Aptian–Albian strata) likely indicates that the dolomitization process affecting both areas is the same and, accordingly, occurred at the same time. In this line, taking into account the dated MVTs calcite in the Maestrat Basin as 63Ma old (Grandia *et al.*, 2000) and according to cross-cutting relationships between replacive dolomite and other diagenetic products (marine, burial and meteoric cements, stylolites, and MVT ore deposits), Gomez-Rivas *et al.* (2014), Martín-Martín *et al.* (2015, 2018) and Yao *et al.* (2020) suggested a Late Cretaceous age for the dolomitization process affecting the Aptian–Albian dolostones of the Benicàssim area, during the post-rift stage of the Maestrat Basin.

The calculated geothermal gradient during the Late Jurassic–Early Cretaceous rifting stage is about 30ºC/Km, which is in the range of typical geothermal gradients in rift settings (Gholamrezaie *et al.*, 2018). This value is consistent with the temperatures indicated by vitrinite reflectance and fluid inclusions in the Mas d'Ascla Formation (upper Kimmeridgian–lowermost Tithonian) from the La Salzedella sub-basin (~27ºC/Km; Rossi *et al.*, 2001; Salas and Permanyer, 2003). This would indicate that during the dolomitization time interval (between the end of the Early Cretaceous and the end of the Late Cretaceous), and according to subsidence curves (Martinez-Abad, 1991; Permanyer and Salas, 2000), the Bovalar Formation limestones reached a burial depth between 1.3 and 3.4km at the La Salzedella sub-basin depocenter (Maestrazgo-1 well). This would correspond to a host rock temperature in the range of 60 to 120ºC, assuming a surface temperature of 20ºC. Fluid inclusions within replacive dolomite of the basin depocenter reveal fluid temperatures between 70 and 120ºC (Table 6), which is consistent with the temperature according to the geothermal gradient. Our data reveals that samples from the depositional highs offer little temperature variations, with a mean value of 97ºC, while those from the La Salzedella sub-basin depocenter display a wider Th range (Table 6).

To account for the dolomitization process, one or more sources of Mg-rich fluids, as well as a suitable driving force for their flow, are required. Potential dolomitizing fluid sources include: i) Lower or Upper Cretaceous seawater infiltrated to the basin (either pristine or concentrated), ii) dissolution of Triassic and Lower Jurassic evaporites, iii) expulsion of connate waters trapped in the underlying marine sediments, fluids expulsed during clay recrystallisation or v) expulsion of basement fluids resulting from mineral transformations.

In terms of the potential fluid volume, seawater infiltration can provide large amounts of fluid to account for the dolomitization process. However, it should be noted that the $\delta^{18}O$ and $^{87}Sr/^{86}Sr$ values, as well as salinities measured from fluid inclusions (16 to 23wt % NaCl equivalent) of the studied dolomite are not consistent with a Lower or Upper Cretaceous pure seawater origin. Accordingly, seawater would have interacted with basin and basement fluids and host rock to acquire a higher salinity and a more radiogenic signature.

Although marine evaporites are abundant in the Triassic–Lower Jurassic units of the Iberian Chain, they mainly consist of gypsum, anhydrite and halite (Bartrina and Hernández, 1990; Bordonaba, 2003; Ortí *et al.*, 1996). Calcium sulphates display low Mg content, below 200ppm (Lu *et al.*, 2002; Playà *et al.*, 1997; Rosell and Ortí, 1992) and Mg is nearly inexistent within the halite lattice. The only Mg-bearing evaporite present is polihalite (Ortí *et al.*, 1996), although it occurs in insufficient amounts to supply enough Mg to account for the large volume of dolomitized carbonates in the basin. Thus, although partial dissolution of Triassic and Lower Jurassic evaporites could explain the more radiogenic $^{87}Sr/^{86}Sr$ ratios of the dolomitizing fluids (Fig. 8), the presence of anhydrite-gypsum minerals cannot account for all the Mg required for dolomitization and only partial dissolution of the underlying carbonate units can potentially be considered.

Another possible source of Mg-rich fluids is trapped connate seawater. The Upper Kimmeridgian–lower Tithonian marls of the Mas d'Ascla Formation are volumetrically insufficient to provide enough fluid to explain the dolostone volume, because these marls are restricted to the more central parts of the Maestrat Basin. Mg-rich fluids can also be related to the expulsion of connate waters derived from compaction of marine Triassic–Lower Jurassic sediments, which could explain the $^{87}Sr/^{86}Sr$ ratios for the studied dolomite (Fig. 8). Triassic units in the Maestrat Basin are lithologically heterogeneous, including clays and sandstones, limestones, dolostones and marine evaporites (gypsum, anhydrite and halite) (Ortí *et al.*, 1996; Salas *et al.*, 2001; Utrilla *et al.*, 1992). Mg remains in the brine during evaporite mineral precipitation, and the brine can become progressively enriched in Mg. Mg-rich brines can be trapped in intergranular pores and in primary fluid inclusions during the growth of halite and gypsum crystals. Nevertheless, effective porosity is typically occluded early and at shallow depths in calcium sulphate and halite deposits by compaction and secondary evaporite cementation. Furthermore, by a burial of 100 meters, halite units are tight and impervious (Casas and

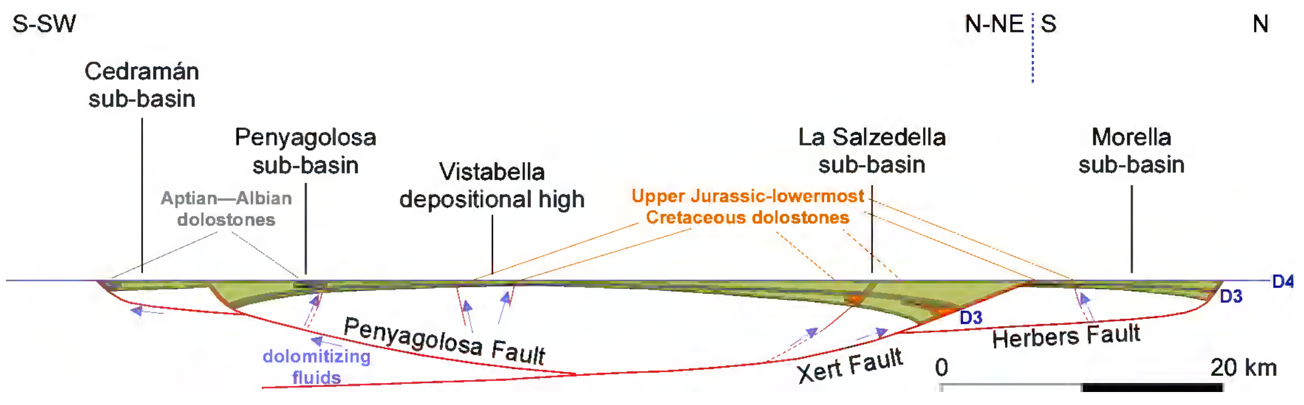

FIGURE 10. Regional cross section at the end of the Early Cretaceous (Albian), showing the structure of the basin, the two regional unconformities D3 and D4, and the conceptual model for the dolomitization of Upper Jurassic–lowermost Cretaceous carbonates (below D3) and Aptian–early Albian carbonates (below D4). The blue arrows illustrate the flow of dolomitizing fluids from below along faults likely mobilized by thermal convection. See Figure 1 for the cross-section location.

Lowenstein, 1989; Warren, 1999). Thus, expulsion of trapped brines in Triassic (and Lower Jurassic) evaporites would have occurred before the deposition of the limestones of the Bovalar Formation. Incorporation of remaining connate water during the carbonate dissolution cannot be considered because the underlying carbonate units were probably already compacted when the Bovalar Formation limestones were dolomitized. Additionally, the signature of such fluid would not be consistent with the oxygen isotope values of the dolostones.

Crystallization water of clay minerals could be expelled during clay recrystallisation (transformation to illite and chlorite) by compaction during burial diagenesis of Triassic clays, also providing a Mg-rich fluid. These mineralogical changes cause the expulsion of OH^- and accompanying ions into solutions, originating a mineralogically homogeneous deposit (mainly consisting of illite and chlorite; Chamley, 1989). However, this transformation cannot be considered a major source of Mg, due to the low volume of fluid that could be produced.

Fluids sourced from the basement, whose volume cannot currently be quantified, could represent another potential source of Mg. These fluids would explain the radiogenic character of the dolomitizing waters, according to their Sr isotope signatures.

Consequently, the most consistent hypothesis for the origin of Mg-rich brines seems to be a combination of different sources, likely consisting of Lower Cretaceous seawater that was infiltrated in the basement and that interacted with underlying carbonate and evaporite units, and potentially with basement rocks. This source could explain the large volume of fluid required to cause dolomitization of the study rocks across the basin, as well as their slightly radiogenic character, and the high Mn and Fe content. The resulting brines, enriched in $^{87}Sr/^{86}Sr$, saline and hot, were capable of migrating upward along faults until they encountered more surficial and permeable horizons suitable for dolomitization (Travé *et al.*, 1998) and potentially arrested by regional unconformities (D3 and D4). This Mg source would fit with those proposed for Aptian–lower Albian dolostones of the Penyagolosa sub-basin based on geochemical mass-balance calculations and reactive transport models (Corbella *et al.*, 2014; Gomez-Rivas *et al.*, 2014).

The only possible driving force for the mobilization of such fluids would be thermal convection, as a consequence of temperature differences resulting from crustal disequilibrium during the rifting period, as proposed by Gomez-Rivas *et al.* (2014) and Martín-Martín *et al.* (2015) for the Penyagolosa sub-basin. In such a system, seawater would have infiltrated into the deeper sectors of the basin, and potentially to the basement, interacting with the rocks there and changing its signature. After some time, the fluids would have been mobilized preferentially along faults due to temperature and salinity differences (buoyancy forces) within convection cells. The regional unconformities D3 and D4 would have acted as seals for dolomitizing fluids at the basin scale, constraining the convection cells and thus the replacement reaction to the underlying rocks below them. In particular, D3 separates the Tithonian–Berriasian dolomitized carbonates of the Bovalar Formation below the unconformity and the freshwater non-dolomitized limestones with charophytes of Valanginian–early Hauterivian above it, while D4 separates the dolomitized carbonates of the Aptian–lowermost Albian Benassal Formation below and the Albian claystones and sandstones of the Escucha Formation above. In such a scenario, the units above the unconformities were more impermeable, acting as seals, and likely blocking the migration of the dolomitizing fluids that ascended along faults, causing the replacement of carbonates just below these two unconformities (Fig. 10). This mechanism allows explaining with the same mechanisms the contemporaneous dolomitization of the Late Jurassic–lowermost Cretaceous carbonates (Humphrey *et al.*, 2022, and this study) and the Aptian–lowermost Albian ones (Corbella *et al.*, 2014; Gomez-Rivas *et al.*, 2014, 2022; Martín-Martín *et al.*, 2013, 2015, 2018; Yao *et al.*, 2020) across the whole Maestrat Basin. The dolomitization temperatures of Upper Jurassic–lowermost Cretaceous dolostones roughly match those according to the geothermal gradient. When warm fluids are mobilized from below they cool down while ascending, so they may react in thermal equilibrium with the host rock. In such case the Upper Jurassic–lowermost Cretaceous dolostones can be considered geothermal (according to the definition of Machel and Lonnee, 2002), while the Aptian–lower Albian ones were defined as hydrothermal in previous studies.

CONCLUSIONS

The study of the Tithonian–Berriasian dolostones cropping out in the Maestrat Basin (Iberian Chain, SE Spain) resulted in the following conclusions:

i) Dolostones are located adjacent to extensional faults striking NE-SW and, in a minor extent, NW-SE and N-S, and dominantly replace limestones of the Bovalar Formation as well as the La Pleta and Loriguilla formations.

ii) Field data indicate that dolostones bodies range from tens of meters to several kilometers in width and reach thicknesses of up to 150m, forming massive, wedge-shaped, and tabular stratabound geometries. Massive wedge-shaped bodies appear attached to fractures and pervasively replace the limestones without any textural and facies control. The stratabound tabular bodies occur away from fractures and replace the host limestones following the bedding, and suggesting facies and textural controls. Occasionally, both bodies appear connected and transitioning from massive wedge-shaped to tabular stratabound geometries out of the fault.

iii) The results indicate that faults acted as conduits for the migration of dolomitizing fluids and thus are interpreted to be the primary control in the replacement reaction. Regional basement fractures are thought to result in larger dolostone bodies containing massive and stratabound parts.

iv) Dolostones from the basin depocenter show significantly lower content in Fe and Mn and slightly more depleted $\delta^{18}O$ compared to dolostones from depositional highs, evidencing the controls of basin architecture on the geochemical composition of fluids.

v) Fluid inclusion data and isotopic/geochemical signatures indicate that dolomitization was driven by saline, slightly radiogenic Mg-rich brines likely derived from seawater that infiltrated the basin and interacted with underlying rocks. These fluids probably circulated in thermal convection cells, rising along faults but confined by regional unconformities (D3, D4), which localized dolomitization to the Jurassic–Cretaceous carbonates beneath them.

ACKNOWLEDGMENTS

We thank Denis Lavoie and Ihsam Al-Aasm for an early review of this manuscript. Mercè Corbella and Miguel Ángel Caja are thanked as reviewers, and Telm Bover as invited editor, for carefully reading the manuscript and providing valuable feedback. This work was supported by the framework of Spanish Projects DGICYT PID2021-122467NB-C22 (funded by Ministerio de Ciencia, Innovación y Universidades/Agencia Estatal de Investigación/Fondo Europeo de Desarrollo Regional, Unión Europea/10.13039/501100011033) and PID-2020-118999GB-I00 (funded by Ministerio de Ciencia, Innovación y Universidades/ Agencia Estatal de Investigación/10.13039/501100011033), and the Grup de Recerca reconegut per la Generalitat de Catalunya, 2021 SGR-Cat 00349 "Geologia Sedimentària".

REFERENCES

Al-Aasm, I., 2003. Origin and characterization of hydrothermal dolomite in the Western Canada Sedimentary Basin. J. Geochem. Explor., 78-79, 9-15.

Allan, J.R., Wiggins, W.D., 1993. Dolomite reservoirs: geochemical techniques for evaluating origin and distribution. Amer. Assoc. Petrol. Geol. Spec. Pub., Tulsa, Oklahoma, U.S.A, 129pp.

Bádenas, B., Salas, R., Aurell, M., 2004. Three orders of regional sea-level changes control facies and stacking patterns of shallow platform carbonates in the Maestrat Basin (Tithonian-Berriasian, NE Spain). Int. J. Earth Sci. (Geol Rundsch), 93, 144-162.

Bartrina, T., Hernández, E., 1990. Las unidades evaporíticas del Triásico del subsuelo del Maestrazgo. In: Ortí, F., Salvany, J.M. (eds.). Formaciones evaporíticas de la Cuenca del Ebro y cadenas periféricas, y de la zona de Levante. Nuevas aportaciones y guía de superficie. ENRESA -Dep. Geoq. Prosp. Petrol. (UB), Barcelona, 34-38.

Black, D.F.B., Mac Quown, W.C., Dettaas, R.J., 1981. The relation of dolomite associated with faults to the stratigraphy and structure of Central Kentucky. Contributions to the Geology of Kentucky. Geological Survey of Professional Paper, 1151-A, A1-A19.

Bordonaba, A.P., 2003. Evolución sedimentaria del Jurásico inferior (Hettangiense-Pliensbachiense) en el sector centrooriental de la Cordillera Ibérica. Ph.D. Thesis. Zaragoza (Spain), Universidad de Zaragoza, 417pp.

Bover-Arnal, T., Guimerà, J., Moreno-Bedmar, J.A., Ferràndez-Cañadell, C., Salas, R., 2024. Aptian major changes in accommodation. New sedimentary evidence from the Maestrat Basin (E Iberia). Sed. Geol., 459, 106546. DOI: https://doi.org/10.1016/j.sedgeo.2023.106546.

Burke, W.H., Denison, R.E., Hetherington, E.A., Koepnick, R.B., Nelson, H.F., Otto, J.B., 1982. Variation of seawater $^{87}Sr/^{86}Sr$ throughout Phanerozoic time. Geology, 10, 516-519.

Caja, M.A., Al-Aasm, I.S., Marfil, R., Tsige, M., Martín-Crespo, T., Salas, R., 2003. Multiphase carbonate cementation related to fractures in the Upper Jurassic limestones, Maestrat Basin (Iberian Range, Spain). Journ. Geochem. Explor., 78-79, 33-38.

Casas, E., Lowenstein, T.K., 1989. Diagenesis of saline pan halite; comparison of petrographic features of modern, Quaternary and Permian halites. J. Sediment. Petrol., 59, 724-739.

Centrella, S., Beaudoin, N.E., Trebucq, C., Hoareau, G., Gomez Rivas, E., Martín-Martín, J.D., Callot, J.-P., 2023a. Textural and chemical evolution during dedolomitization: a case study of the Benassal Formation, Maestrat Basin, Spain. Marine and Petroleum Geology, 153, 106290.

Centrella, S., Hoareau, G., Beaudoin, N.E., Motte, G., Lanari, P., Piccoli, F., Callot, J.-P., Gomez-Rivas, E., Martín-Martín, J.D., 2023b. Estimating the fluid composition after dolomitization using mass balance equation: comparison of examples from Spain, Canada and France. Global and Planetary Change, 220, 104016.

Chamley, H., 1989. Clay sedimentology. Springer-Verlag, Germany, 623pp.

Churcher, P.L., Majid, A.H., 1989. Similarities between the Tangent-Wabamun type play of the Alberta Basin and the Albion-Scipio type play of the Michigan Basin. Bull. Can. Petrol. Geol., 37, 241-245.

Corbella, M., Gomez-Rivas, E., Martín-Martín, J.D., Stafford, S.L., Teixell, A., Griera, A., Travé, A., Cardellach, E., Salas, R., 2014. Insights to controls on dolomitization by means of reactive transport models applied to the Benicàssim case study (Maestrat Basin, eastern Spain). Petroleum Geoscience, 20(1), 41-54.

Crawford, M.L., 1981. Phase equilibria in aqueous fluid inclusions. In: Hollister, L.S., Crawford, M.L. (eds.). Short course in fluid inclusions: Applications to petrology. Miner. Assoc. Canada, 6, 75-100.

Davies, D.W., Lowenstein, T.K., Spencer, R.J., 1990. Melting behaviour of fluid inclusions in laboratory-grown halite crystals in the systems NaCl-H_2O, NaCl-KCl-H_2O, NaCl-$MgCl_2$-H_2O. and NaCl-$CaCl_2$-H_2O. Geochim. Cosmochim. Acta, 54, 591-601.

Davies, G.R., Smith, L.S., 2006. Structurally controlled hydrothermal dolomite reservoir facies: An overview. AAPG Bull, 90, 1641-1690.

Dewit, J., Foubert, A., El Desouky, H.A., Muchez, P., Hunt, D., Vanhaecke, F., Swennen, R., 2014. Characteristics, genesis and parametres controlling the development of a large stratabound HTD body at Matienzo (Ramales Platform, Basque-Cantabrian Basin, northern Spain). Marine and Petroleum Geology, 55, 6-25.

Escorcia, L., Gomez-Rivas, E., Daniele, L., Corbella, M., 2013. Dedolomitization and reservoir quality, insights from reactive transport modelling. Geofluids, 13(2), 221-231.

Esteban, M., Torrescusa, T., Lukito, P., Solla, C., De Viguera, C., Riaza, C., Lara, L.M., Soriano, S., 2005. Facies sísmicas y diagénesis tardía en almacenes carbonatados. In: Martínez del Olmo, W. (ed.). XXV Aniversario. Asociación de Geólogos y Geofísicos Españoles del Petróleo, 1-17.

Faure, G., Asserreto, R., Tremba, E.L., 1978. Strontium isotope composition of marine carbonates of Middle Triassic to Early Jurassic age, Lombardic Alps, Italy. Sedimentology, 25, 523-543.

Fernàndez, M., Marzán, I., Correia, A., Ramalho, E., 1998. Heat flow, heat production, and lithospheric thermal regime in the Iberian Peninsula. Tectonophysics, 291, 29-53.

Garreau, B., Charpal, O.L., Montadert, L., Gubler, G., Rouge, P.E., Baron, G.A., Favre, J.H., 1959. Contribution française a l'etude de la dolomitization. France, Internal Report of the Institut Française du Pétrole, Section I-Paper 3, 53-80.

Gasparrini, M., Bechstädt, T., Boni, M. 2006. Massive hydrothermal dolomites in the southwestern Cantabrian Zone (Spain) and their relation to the Late Variscan evolution. Marine and Petroleum Geology, 23(5), 543-568.

Gasparrini, M., López-Cilla, I., Blázquez-Fernández, S., Rosales, I., Lerat, O., Martín-Chivelet, J., Doligez, B., 2017. A Multidisciplinary Modeling Approach to Assess Facies-Dolomitization-Porosity Interdependence in a Lower Cretaceous Platform (Northern Spain). SEPM Special Publications, 109, 130-53. DOI: https://doi.org/10.2110/sepmsp.109.07.

Gholamrezaie, E., Scheck-Wenderoth, M., Sippel, J., Strecker, M.R., 2018. Variability of the geothermal gradient across two differently aged magma-rich continental rifted margins of the Atlantic Ocean: the Southwest African and the Norwegian margins. Solid Earth, 9, 139-158. DOI: https://doi.org/10.5194/se-9-139-2018.

Gomez-Rivas, E., Corbella, M., Martín-Martín, J.D., Stafford, S.L., Teixell, A., Bons, P.D., Griera, A., Cardellach, E., 2014. Reactivity of dolomitizing fluids and Mg source evaluation of fault-controlled dolomitization at the Benicassim outcrop analogue (Maestrat Basin, E Spain). Marine and Petroleum Geology, 55, 26-42.

Gomez-Rivas, E., Martín-Martín, J.D., Bons, P.D., Koehn, D., Griera, A., Travé, A., Llorens, M.-G., Humphrey, E., Neilson, J., 2022. Stylolites and stylolite networks as primary controls on the geometry and distribution of carbonate diagenetic alterations. Marine and Petroleum Geology, 136, 105444.

Gradstein, F.M., Ogg, J.G., Smith, A.G., Agterberg, F.P., Bleeker, W., Cooper, R.A., Davydov, V., Gibbard, P., Hinnov, L.A., House, M.R., Lourens, L., Luterbacher, H.P., McArthur, J., Melchin, M.J., Robb, L.J., Shergold, J., Villeneuve, M., Wardlaw, B.R., Ali, J., Brinkhuis, H., Hilgen, F.J., Hooker, J., Howarth, R.J., Knoll, A.H., Laskar, J., Monechi, S., Plumb, K.A., Powell, J., Raffi, I., Röhl, U., Sadler, P., Sanfilippo, A., Schmitz, B., Shackleton, N.J., Shields, G.A., Strauss, H., Van Dam, J., van Kolfschoten, T., Veizer, J., Wilson, D., 2004. A Geologic Time Scale 2004. Cambridge University Press, 589pp.

Grandia, F., Asmerom, Y., Getty, S., Cardellach, E., 2000. U–Pb dating of MVT ore-stage calcite: implications for fluid flow in a Mesozoic extensional basin from Iberian Peninsula. Journal of Geochemical Exploration, 69-70, 377-380.

Grandia, F., Cardellach, E., Canals, A., Banks, D.A., 2003. Geochemistry of the fluids related to epigenetic carbonate-hosted Zn-Pb deposits in the Maestrat Basin, Eastern Spain: Fluid inclusion and isotope (Cl, C, O, S, Sr) evidence. Econ. Geol., 98, 933-954.

Green, D.G., Mountjoy, E.W., 2005. Fault and conduit controlled burial dolomitization of the Devonian west-central Alberta Deep Basin. Bull. Can. Petrol. Geol., 53, 101-129.

Gregg, J.M., Sibley, D.F., 1984. Epigenetic dolomitization and the origin of saddle dolomite. Journal of Sedimentary Petrology, 54, 908-931.

Groetsch, J., Vahrenkamp, V., 1995. Can carbon isotopes be used as a stratigraphic tool in Mid-Cretaceous shallow water carbonates? Amer. Assoc. Petrol. Geol. Bull., 79, 1218.

Hirani, J., Bastesen, E., Boyce, A., Corlett, H., Gawthorpe, R., Hollis, C., John, C. M., Robertson, H., Rotevatn, A., Whitaker, F., 2018. Controls on the formation of stratabound dolostone bodies, Hammam Faraun Fault block. Gulf of Suez. Sedimentology, 65(6), 1973-2002.

Hollis, C., Bastesen, E., Boyce, A., Corlett, H., Gawthorpe, R., Hirani, J., Rotevatn, A., Whitaker, F., 2017. Fault-controlled dolomitization in a rift basin. Geology, 45(3), 219-222.

Holser, W.T., Magaritz, M., 1987. Events near the Permian-Triassic boundary. Mod. Geol., 11, 180.

Humphrey, E., Gomez-Rivas, E., Neilson, J., Martín-Martín, J.D., Healy, D., Yao S., Bons, P.D., 2020. Quantitative analysis of stylolite networks in different platform carbonate facies. Marine and Petroleum Geology, 114, 104203.

Humphrey, E., Gomez-Rivas, E., Martín-Martín, J.D., Neilson, J., Salas, R., Guimerà, J., 2022. Depositional and Structural Controls on a Fault-Related Dolostone Formation (Maestrat Basin, E Spain). Basin Research, 34(2), 961-990. DOI: https://doi.org/10.1111/bre.12647

Jenkyns, H.C., Jones, C.E., Gröcke, D.R., Hesselbo, S.P., Parkinson, D.N., 2002. Chemostratigraphy of the Jurassic System: applications, limitations and implications for palaeoceanography. J. Geol. Soc. London, 159, 351-378.

Jones, C.E., Jenkyns, H.C., Coe, A.L., Hesselbo, S.P., 1994. Strontium isotope variations in Jurassic and Cretaceous seawater. Geochim. Cosmochim. Acta, 58, 3061-3074.

Jones, R.M.P., 1980. Basinal isostatic adjustment faults and their Petroleum significance. Bull. Can. Petrol. Geol., 28, 211-251.

Koepnick, R.B., Burke, W.H., Denison, R.E., Hetherington, E.A., Nelson, H.F., Otto, J.B., Waite, L.E., 1985. Construction of the seawater $^{87}Sr/^{86}Sr$ curve for the Cenozoic and Cretaceous: supporting data. Chem. Geol., 58, 55-81.

Koepnick, R.B., Denison, R.E., Burke, W.H., Hetherington, E.A., Dahl, D.A., 1990. Construction of the Triassic and Jurassic portion of the Phanerozoic curve of seawater $^{87}Sr/^{86}Sr$. Chem. Geol., 80, 327-349.

Korte, C., Kozur, H.W., Bruckschen, P., Veizer, J., 2003. Strontium isotope evolution of Late Permian and Triassic seawater. Geochim. Cosmochim. Acta, 67, 47-62.

Lapponi, F., Casini, G., Sharp, I., Blendinger, W., Fernandez, N., Romaire, I., Hunt, D., 2011. From outcrop to 3D modelling: a case study of a dolomitized carbonate reservoir, Zagros Mountains, Iran. Pet. Geosci., 17(3), 283-307.

Lapponi, F., Bechstaedt, T., Boni, M., Banks, D.A., Schneider, J., 2014. Hydrothermal dolomitization in a complex geodynamic setting (Lower Palaeozoic, northern Spain). Sedimentology, 61(2), 411-443.

Lomando, A.J., Harris, P.M., Orlopp, D.E., 1993. Casablanca field, Tarragona Basin, offshore Spain: a karsted carbonate reservoir. In: Fritz, R.D., Wilson, J.L., Yurewicz, D.A. (eds.). Paleokarst related hydrocarbon reservoirs. SEPM Core Workshop, 18, 201-225.

Lu, F.H., Meyers, W.J., Hanson, G.N., 2002. Trace elements and environmental significance of Messinian gypsum deposits, the Nijar Basin, southeastern Spain. Chem. Geol., 192, 149-161.

Machel, H.G., 2004. Concepts and models of dolomitization: a critical reappraisal. In: Braithwaite, C.J.R., Rizzi, G., Darke, G. (eds.). The Geometry and Petrogenesis of Dolomite Hydrocarbon Reservoirs. Geol. Soc. London Spec. Publ., 235, 7-63.

Machel, H.G., Mountjoy, E.W., 1987. Pervasive dolomitization of the Devonian carbonates of Western Canada. Bull. Can. Petrol. Geol., 35, 143-158.

Machel, H., Lonnee, J., 2002. Hydrothermal dolomite—A product of poor definition and imagination. Sedimentary Geology, 152, 163-171.

Malone, M.J., Baker, P.A., Burns, S.J., 1996. Hydrothermal dolomitization and recrystallization of Dolomite Breccias from the Miocene Monterey Formation, Tepusquet Area, California. J. Sediment. Res., 66, 976-990.

Marfil, R., Caja, M.A., Tsige, M., Al-Aasm, I.S., Martín-Crespo, T., Salas, R., 2005. Carbonate-cemented stylolites and fractures in the Upper Jurassic limestones of the Eastern Iberian Range, Spain: A record of palaeofluids composition and thermal history. Sedimen. Geol., 178, 237-25.

Martín-Chivelet, J., López-Gómez, J., Aguado, R., Arias, C., Arribas, J., Arribas, M.E., Aurell, M., Bádenas, B., Benito, M.I., Bover-Arnal, T., Casas-Sainz, A., Castro, J.M., Coruña, F., de Gea, G.A., Fornós, J.J., Fregenal-Martínez, M., García-Senz, J., Garófano, D., Gelabert, B., Giménez, J., González-Acebrón, J., Guimerà, J., Liesa, C.L., Mas, R., Meléndez, N., Molina, J.M., Muñoz, J.A., Navarrete, R., Nebot, M., Nieto, L.M., Omodeo-Salé, S., Pedrera, A., Peropadre, C., Quijada, I.E., Quijano, M.L., Reolid, M., Robador, A., Rodríguez-López, J.P., Rodríguez-Perea, A., Rosales, I., Ruiz-Ortiz, P.A., Sàbat, F., Salas, R., Soria, A.R., Suarez-Gonzalez, P., Vilas, L., 2019. The Late Jurassic–Early Cretaceous Rifting. In: Quesada, C., Oliveira, J.T. (eds.). The Geology of Iberia: A Geodynamic Approach. Volume 3: The Alpine Cycle. Heidelberg, Springer, 60-63. DOI: https://doi.org/10.1007/978-3-030-11295-0

Martín-Martín, J.D., Gomez-Rivas, E., Bover-Arnal, T., Travé, A., Salas, R., Moreno-Bedmar, J.A., Tomás, S., Corbella, M., Teixell, A., Vergés, J., Stafford, S.L., 2013. The Upper Aptian to Lower Albian syn-rift carbonate succession of the southern Maestrat Basin (Spain): Facies architecture and fault-controlled stratabound dolostones. Cretaceous Research, 41, 217-236.

Martín-Martín, J.D., Travé, A., Gomez-Rivas, E., Salas, R., Sizun, J.P., Vergés, J., Corbella, M., Stafford, S.L., Alfonso, P., 2015. Fault-controlled and stratabound dolostones in the Late Aptian–earliest Albian Benassal Formation (Maestrat Basin, E Spain): Petrology and geochemistry constraints. Marine and Petroleum Geology, 65, 83-102.

Martín-Martín, J.D., Gomez-Rivas, E., Gómez-Gras, D., Travé, A., Ameneiro, R., Koehn, D., Bons, P.D., 2018. Activation of stylolites as conduits for overpressured fluid flow in dolomitized platform carbonates. London, The Geological Society, 459(1, Special Publications), 157-176.

Martinez-Abad, J.L., 1991. Cuenca del Maestrazgo. Correlación de sondeos I-I'. En: Estudio geológico del Maestrazgo y de la mitad meridional de los Catalánides (F. López, coord.). INYPSA-IGME, unpublished.

McKenzie, D.P., 1978. Some remarks on the development of sedimentary basins. Earth and Planetary Science Letters, 40, 25-32.

Morrison, J.O., Veizer, J., 1990. Belemnite geochemistry: an indicator of secular and environmental variation of Cretaceous seawater. Geol. Soc. Amer. Bull., Abstracts with Programs, A116.

Mozafari, M., Swennen, R., Balsamo, F., El Desouky, H., Storti, F., Taberner, C., 2019. Fault-controlled dolomitization in the Montagna dei Fiori Anticline (Central Apennines, Italy): record of a dominantly pre-orogenic fluid migration. Solid Earth, 10(4), 1355-1383.

Muñoz-Cervera, M.C., Cañaveras, J.C., 2023. Diagenetic Study of Marrón Emperador Ornamental Stone (Upper Cretaceous, SE Spain). Applied Sciences, 13(9), 5470.

Nadal, J., 2001. Estudi de la dolomitització del Juràssic superior-Cretaci inferior de la Cadena Ibèrica oriental i la Cadena Costanera Catalana: relació amb la segona etapa de rift mesozoica. PhD Thesis. Barcelona, Universitat de Barcelona, 445pp.

Nader, F.H., Swennen, R., 2004. Petroleum prospects of Lebanon: some remarks from sedimentological and diagenetic studies of Jurassic carbonates. Marine and Petroleum Geology, 21(4), 427-441.

Ortí, F., García-Veigas, J., Rosell, L., Jurado, M.J., Utrilla, R., 1996. Formaciones triásicas en la Península Ibérica: caracterización petrológica y geoquímica. Cuadernos de Geología Ibérica, 20, 13-35.

Permanyer, A., Salas, R., 2000. Thermal modeling and geochemical constraints in the Late Jurassic of the southern Iberian Chain (NE Spain). In: Tröndade, L.A., Macedo, A.C., Barbanir, S.M. (eds.). New Perspectives on Organic Geochemistry for the third Millenium. Proceedings of 7th Latin-american Congress on Organic Geochemistry, 179-182.

Permanyer, A., Salas, R., 2005. Integrated thermal model, diagenetic history and oil correlation in Western Mediterranean, Spain. IV ALAGO Workshop-Basin Modeling, Buenos Aires, Argentina.

Pirrie, D., Marshall, J.D., 1990. High-paleolatitude Late Cretaceous paleotemperatures: new data from James Ross Island, Antarctica. Geology, 18, 31-34.

Playà, E., Rosell, L., Ortí, F., 1997. Las evaporitas de la cuenca neógena de Fortuna (Murcia): Aspectos diagenéticos y geoquímicos. Cuadernos de Geología Ibérica, 22, 191-211.

Playà, E., Travé, A., Caja, M.A., Salas, R., Martín-Martín, J.D., 2010. Diagenesis of the Amposta offshore oil reservoir (Amposta Marino C2 well, Lower Cretaceous, Valencia Trough, Spain). Geofluids, 10, 314-333.

Rodríguez-Morillas, N., Playà, E., Travé, A., Martín-Martín, J.D., 2013. Casablanca oil field, Valencia Trough, offshore Spain: Diagenetic processes in a carbonate reservoir. Geologica Acta, 11, 195-214

Rosell, L., Ortí, F., 1992. Geochemical characteristics and facies analysis of a Miocene lacustrine gypsum deposit (Calatayud basin, Zaragoza, Spain). IGCP-324 Glopals, Annual Meeting, Abstracts, 39-41.

Rossi, C., Goldstein, R.H., Marfil, R., Salas, R., Benito, M.I., Permanyer, A., de la Peña, J.A., Caja, M.A., 2001. Diagenetic and oil migration history of the Kimmeridgian Ascla Formation, Maestrat Basin, Spain. Mar. Petrol. Geol., 18, 287-306.

Roure, F., Swennen, R., Schneider, F., Faure, J.L., Ferket, H., Guilhaumou, N., Osadetz, K., Robion, P., Vandeginste, V., 2005. Incidence and Importance of Tectonics and Natural Fluid Migration on Reservoir Evolution in Foreland Fold-and-Thrust Belts. Oil & Gas Science Technology - Rev. IPF, 60, 67-106.

Rustichelli, A., Iannace, A., Tondi, E., Di Celma, C., Cilona, A., Giorgioni, M., Parente, M., Girundo, M., Invernizzi, C., 2017. Fault-controlled dolomite bodies as palaeotectonic indicators and geofluid reservoirs: New insights from Gargano Promontory outcrops. Sedimentology, 64(7), 1871-1900.

Salas, R., 1987. El Malm i el Cretaci inferior entre el Massís del Garraf i la Serra d'Espadà. Ph.D. Thesis. Barcelona, Universitat de Barcelona, 345pp.

Salas, R., Casas, A., 1993. Mesozoic extensional tectonics, stratigraphy and crustal evolution during the Alpine cycle of the eastern Iberian basin. Tectonophysics, 228, 33-55.

Salas, R., Permanyer, A., 2003. Evidencias de generación de hidrocarburos en la formación de margas del Mas d'Ascla (Jurásico superior, Cadena Ibérica oriental) y su relación con el campo de Amposta de la Cuenca de Tarragona. Boletín Geológico y Minero, 114, 75-86.

Salas, R., Guimerà, J., Mas, R., Martín-Closas, C., Meléndez, A., Alonso, A., 2001. Evolution of the Mesozoic Central Iberian Rift System and its Cainozoic inversion (Iberian Chain). In: Ziegler, P.A., Cavazza, W., Robertson, A.H.F., Crasquin-Soleau, S. (eds.). Peri-Tethys Memoir 6: Per-Tethyan Rift/ Wrench Basins and Passive Margins. Paris, Mém. Mus. Natn. Hist. Nat., 186, 145-185.

Seemann, U., Pümpin, V.F., Casson, N., 1990. Amposta Oil Field. AAPG Treatise of Petroleum Geology, Atlas of Oil and Gas Fields, A-017, 1-20.

Sharp, I., Gillespie, P., Morsalnezhad, D., Taberner, C., Karpuz, R., Vergés, J., Horbury, A., Pickard, N., Garland, J., Hunt, D., 2010a. Stratigraphic architecture and fracture-controlled dolomitization of the Cretaceous Khami and Bangestan groups: an outcrop case study, Zagros Mountains. Iran. London, The Geological Society, 329(1, Special Publications), 343-396.

Sharp, I., Hovorka, S.D., Kerans, C., 2010b. Dolomitization and fluid flow in the Upper San Andres Formation: insights from outcrop and subsurface data, Guadalupe Mountains and subsurface west Texas, USA. AAPG Bulletin, 94(4), 561-590.

Shelton, K.L., Hendry, J.P., Gregg, J.M., Truesdale, J.P., Somerville, I.D., 2019. Fluid circulation and fault- and fracture-related diagenesis in Mississippian syn-rift carbonate rocks on the northeast margin of the metalliferous Dublin Basin, Ireland. Journal of Sedimentary Research, 89(6), 508-536.

Sheperd, T.J., Rankin, A.H., Alderton, D.H.M., 1985. A practical guide to fluid inclusion studies. Blackie, 239pp.

Stacey, J., Corlett, H., Holland, G., Koeshidayatullah, A., Cao, C., Swart, P., Crowley, S., Hollis, C., 2021. Regional fault-controlled shallow dolomitization of the Middle Cambrian Cathedral Formation by hydrothermal fluids fluxed through a basal clastic aquifer. GSA Bulletin, 133(11-12), 2355-2377.

Travé, A., Calvet, F., Soler, A., Labaume, P., 1998. Fracturing and fluid migration during Palaeogene compression and Neogene extension in the Catalan Coastal Ranges, Spain. Sedimentology, 45, 1063-1082.

Utrilla, R., Pierre, C., Ortí, F., Pueyo, J.J., 1992. Oxygen and sulphur isotope compositions as indicators of the origin of Mesozoic and Cenozoic evaporites from Spain. Chem. Geol. (Isotope Geosc. Sect.), 102, 229-244.

Vandeginste, V., John, C.M., van de Flierdt, T., Cosgrove, J.W., 2013. Linking process, dimension, texture, and geochemistry in dolomite geobodies: A case study from Wadi Mistal (northern Oman). AAPG Bulletin, 97(7), 1181-1207.

Veizer, J., Buhl, D., Diener, A., Ebneth, S., Podlaha, O.G., Bruckschen, P., Jasper, T., Korte, C., Schaaf, M., Ala, D., Azmy, K., 1997. Strontium isotope stratigraphy: potential resolution and event correlation. Palaeogeogr. Palaeoclimatol. Palaeoecol., 132, 65-77.

Veizer, J., Compston, W., 1974. $^{87}Sr/^{86}Sr$ composition of seawater during the Phanerozoic. Geochim. Cosmochim. Acta, 38, 1460-1484.

Warren, J., 1999. Evaporites. Their Evolution and Economics. Great Britain, Blackwell Science, 438pp.

Warren, J., 2000. Dolomite: Occurrence, Evolution and Economically Important Associations. Earth-Science Reviews, 52, 1-81. DOI: https://doi.org/10.1016/S0012-8252(00)00022-2

Wilson, E.N., Hardie, L.A., Phillips, O.M., 1990. Dolomitization front geometry, fluid flow patterns, and the origin of massive dolomite: the Triassic Latemar buildup, northern Italy. American Journal of Science, 290(7), 741-796.

Wilson, M.E., Evans, M.J., Oxtoby, N.H., Nas, D.S., Donnelly, T., Thirlwall, M., 2007. Reservoir quality, textural evolution, and origin of fault-associated dolomites. AAPG Bulletin, 91(9), 1247-1272.

Yao, S., Gomez-Rivas, E., Martín-Martín, J.D., Gómez-Gras, D., Travé, A., Griera, A., Howell, J.A., 2020. Fault-controlled dolostone geometries in a transgressive–regressive sequence stratigraphic framework. Sedimentology, 67(6), 3290-3316.

Zwart. E.W., Touret, J.L.R., 1994. Melting behaviour and composition of aqueous fluid inclusions in fluorite and calcite: applications within the system H_2O-$CaCl_2$-NaCl. Eur. J. Mineral, 6, 773-786.

Manuscript received July 2025;
revision accepted October 2025;
published Online December 2025.